# A study of Galactic Plane *Planck* Galactic cold clumps observed by SCOPE and the JCMT Plane Survey

D. J. Eden [1]★ Tie Liu,[2] T. J. T. Moore,[3] J. Di Francesco,[4,5] G. Fuller [6] Kee-Tae Kim,[7,8] Di Li [9,10]
S.-Y. Liu,[11] R. Plume,[12] Ken'ichi Tatematsu [13,14] M. A. Thompson [15] Y. Wu,[16] L. Bronfman,[17]
H. M. Butner,[18] M. J. Currie,[19,20] G. Garay,[17] P. F. Goldsmith,[21] N. Hirano,[11] D. Johnstone,[4,5] M. Juvela,[22]
S.-P. Lai,[11,23,24,25] C. W. Lee,[7,8] E. E. Mannfors,[22] F. Olguin,[25] K. Pattle,[26] Geumsook Park,[7]
D. Polychroni,[27] M. Rawlings,[28] A. J. Rigby,[15] P. Sanhueza,[29,30] A. Traficante,[31] J. S. Urquhart,[32]
B. Weferling,[33] G. J. White[34,19] and R. K. Yadav[35]

*Affiliations are listed at the end of the paper*

## ABSTRACT

We have investigated the physical properties of *Planck* Galactic Cold Clumps (PGCCs) located in the Galactic Plane, using the JCMT Plane Survey (JPS) and the SCUBA-2 Continuum Observations of Pre-protostellar Evolution (SCOPE) survey. By utilizing a suite of molecular-line surveys, velocities, and distances were assigned to the compact sources within the PGCCs, placing them in a Galactic context. The properties of these compact sources show no large-scale variations with Galactic environment. Investigating the star-forming content of the sample, we find that the luminosity-to-mass ratio ($L/M$) is an order of magnitude lower than in other Galactic studies, indicating that these objects are hosting lower levels of star formation. Finally, by comparing ATLASGAL sources that are associated or are not associated with PGCCs, we find that those associated with PGCCs are typically colder, denser, and have a lower $L/M$ ratio, hinting that PGCCs are a distinct population of Galactic Plane sources.

**Key words:** surveys – stars: formation – ISM: clouds – submillimetre: ISM.

## 1 INTRODUCTION

Star formation occurs across the Galaxy, but a large fraction occurs within the Galactic Plane. Milky Way-wide surveys have revealed that the material needed to form stars is almost ubiquitous across the Galactic Plane, such as the molecular gas (e.g. Dame, Hartmann & Thaddeus 2001) or the dust tracing the denser structures (e.g. Molinari et al. 2016), along with the *Planck* Galactic Cold Clumps (PGCCs; Planck Collaboration XXIII 2011, XXVIII 2016). The *Planck* survey sought to map the cosmic microwave background, but in the process of doing so, also mapped the foreground emission. Whilst removing this emission, over 13 000 PGCCs were identified across all Galactic environments, with a significant fraction (∼ 20 per cent) within ±2° of the mid-plane and a further ∼ 20 per cent within ±5°. Follow-up studies of these PGCCs have shown that, although they house the right physical conditions for star formation such as low-dust temperatures (Planck Collaboration XXVIII 2016), CO (e.g. Zhang et al. 2016), dense-gas tracers such as HCN, HCO⁺, N₂H⁺, and NH₃ (e.g. Yuan et al. 2016; Kim et al. 2020; Yi et al. 2021; Fehér et al. 2022; Berdikhan. et al. 2024), they have low levels of star-formation activity (Tang et al. 2018; Yi et al. 2018;

Zhang et al. 2018) and are more quiescent and less evolved than the typical star-forming region (Wu et al. 2012; Liu, Wu & Zhang 2013; Xu et al. 2024). Adding to this, any correlation with young stellar objects tends to the youngest protostellar stages (Juvela et al. 2018).

Recent follow-up observations with interferometers (e.g. ALMA) toward PGCCs in the Orion Giant Molecular Clouds have found that a large fraction of PGCCs contain centrally concentrated, high-density prestellar cores (Dutta et al. 2020; Sahu et al. 2021, 2023; Hirano et al. 2024) and/or young stellar objects with very collimated outflows (Dutta et al. 2020, 2022, 2024; Jhan et al. 2022). The cold and dense cores inside PGCCs also show high deuterium fractions of molecules (Kim et al. 2020; Tatematsu et al. 2021). These observational results indicate that PGCCs may represent the very early stages in star formation, albeit in a nearby star-forming region.

The physical state of the PGCCs thus makes them intriguing as a potential tracer of the earliest stages of star formation. This leads to two questions: are PGCCs significantly different from other star-forming Galactic Plane sources not associated with PGCCs, and do their properties vary as a function of Galactic environment? Galactic environments vary widely. Within the Galactic Centre, the conditions are much more extreme and akin to those in the early universe (i.e. $z \sim 2$–3; Kruijssen & Longmore 2013), whilst in the Outer Galaxy there is a significantly lower metallicity (e.g. Netopil et al. 2022) and radiation field (e.g. Popescu et al. 2017). Galactic-scale studies have

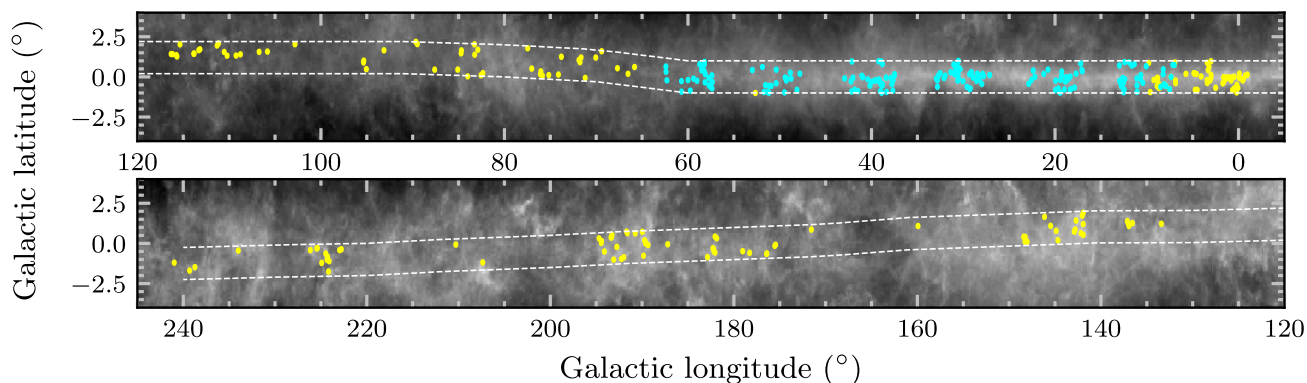★ E-mail: david.eden@armagh.ac.uk

**Figure 1.** The observed PGCCs in the Galactic Plane. The cyan circles represent the sources from the JPS (Eden et al. 2017), whilst the yellow circles are those observed within the SCOPE survey (Eden et al. 2019). The white dashed lines are the extent of the Galactic Plane considered, as derived from the Hi-GAL survey (Schisano et al. 2020). The background image is the *Planck* dust opacity map (Planck Collaboration XI 2014).

indicated that, once a molecular cloud or dense clump forms, the star formation proceeds with the same average efficiency regardless of Galactic environment (e.g. Eden et al. 2012, 2013, 2021; Ragan et al. 2018; Urquhart et al. 2021, 2022). It is, also, important to know if these environmental differences can be detected in the physical properties of some of the youngest dust concentrations in our Galaxy, and whether these differences are imprinted in the ongoing star formation.

This paper is organized as follows: Section 2 introduces the two James Clerk Maxwell Telescope (JCMT) surveys whose catalogues are used for the forthcoming analysis. Sections 3 and 4 introduce the radial-velocity and distance determinations, respectively, whilst Section 5 contains the Galactic distribution of the PGCCs. Sections 6 and 7 address the physical properties of the whole sample and the star-forming content, respectively. Section 8 addresses the differences in the PGCC sample compared to other Galactic Plane sources by utilizing data from the APEX Telescope Large Area Survey of the Galaxy (ATLASGAL; Schuller et al. 2009), and Section 9 summaries the work and states our conclusions.

## 2 SCUBA-2 DATA

The Galactic Plane PGCCs observed at the JCMT with Submillimetre Common-User Bolometer Array 2 (SCUBA-2; Holland et al. 2013) in the 850-μm continuum are contained within two surveys. The first 174 PGCCs were observed as part of the JCMT Plane Survey (JPS; Moore et al. 2015; Eden et al. 2017), which is one of the JCMT Legacy Surveys (Chrysostomou 2010). The JPS was a targeted, yet unbiased, survey of the Galactic Plane, observing equally spaced regions covering approximately $5° × 1.7°$ centred at $\ell = 10°, 20°, 30°, 40°, 50°,$ and $60°$. The SCUBA-2 Continuum Observations of Pre-protostellar Evolution (SCOPE; Liu et al. 2018; Eden et al. 2019) survey observed PGCCs in the Galactic Plane outside of the JPS regions. The SCOPE survey observed 204 Galactic Plane PGCCs.

Another JCMT Legacy Survey, the SCUBA-2 ambitious Sky Survey (SASSy; MacKenzie et al. 2011; Nettke et al. 2017; Thompson et al., in preparation) has observed the Galactic Plane with SCUBA-2. However, its rms sensitivity does not reach the required threshold of $6\,\mathrm{mJy\,beam^{-1}}$, which was the desired rms of the SCOPE survey, and, as such, SASSy is not used in this work.

In this study, we have only considered PGCCs that were found within the latitude range of the *Herschel* infrared Galactic Plane Survey (Hi-GAL; Molinari et al. 2010, 2016). Hi-GAL followed the

warp of the Galaxy (Schisano et al. 2020). The distribution of the observed PGCCs is displayed in Fig. 1.

### 2.1 Compact source extraction

Compact sources were extracted from within each of the JPS and SCOPE surveys using the FELLWALKER (Berry 2015) algorithm. A full explanation of the processes used in each survey can be found in Eden et al. (2017, 2019). JPS and SCOPE contained 7813 and 3528 compact sources, respectively.

Due to the targeted nature of the SCOPE survey, the PGCCs were observed using the CV Daisy mode of SCUBA-2 (Bintley et al. 2014), compared to the pong3600 maps used in the JPS. The CV Daisy mode is most suitable for compact sources, and produced an rms of $6\,\mathrm{mJy\,beam^{-1}}$ in the central-most 3 arcmin, and an rms comparable to the pong3600 maps in the JPS out to a radius of 6 arcmin ($43.9\,\mathrm{mJy\,beam^{-1}}$ in SCOPE compared to 25–$31\,\mathrm{mJy\,beam^{-1}}$ in JPS; Eden et al. 2017, 2019). Therefore, we extracted all compact sources in the JPS catalogue within 6 arcmin of any catalogued PGCC (Planck Collaboration XXIII 2011, XXVIII 2016). This accounted for 1447 compact sources associated with 148 PGCCs, with 26 PGCCs undetected. The Galactic Plane PGCCs from the SCOPE catalogue contained 1731 compact sources, distributed across 169 PGCCs with a 35 undetected PGCCs.

## 3 RADIAL-VELOCITY DETERMINATION

To determine the distance to each PGCC, and therefore Galactic environment and physical properties, the radial velocity of the source compared with the local standard of rest ($v_{\mathrm{lsr}}$) is required. This velocity can then be compared with a Galactic rotation model (e.g. Brand & Blitz 1993; Reid et al. 2014). The velocities for the Galactic Plane PGCCs are available in a suite of molecular-line Galactic Plane surveys, namely the Galactic Ring Survey (GRS, $^{13}$CO $J = 1 − 0$; Jackson et al. 2006); the CO Heterodyne Inner Milky Way Plane Survey (CHIMPS, $^{13}$CO/C$^{18}$O $J = 3 − 2$; Rigby et al. 2016); CHIMPS2 ($^{12}$CO/$^{13}$CO/C$^{18}$O $J = 3 − 2$; Eden et al. 2020); the CO High Resolution Survey (COHRS, $^{12}$CO $J = 3 − 2$; Dempsey, Thomas & Currie 2013; Park et al. 2023); the FOREST Unbiased Galactic Plane Imaging Survey (FUGIN, $^{12}$CO/$^{13}$CO/C$^{18}$O $J = 1 − 0$; Umemoto et al. 2017); Structure, excitation, and dynamics of the inner Galactic interstellar medium (SEDIGISM, $^{13}$CO/C$^{18}$O $J = 2 − 1$; Schuller et al. 2017); and Milky Way Imaging Scroll Painting (MWISP, $^{12}$CO/$^{13}$CO/C$^{18}$O $J = 1 − 0$; Su et al. 2019).

To obtain these velocities, the spectra were inspected at the position of the relevant PGCC. All the compact sources extracted from the JPS and SCOPE surveys (Eden et al. 2017, 2019) are assumed to have the same velocity as the associated PGCC. This process was completed for all surveys that had coverage at the position of a PGCC. The spectra were inspected in decreasing critical-density order. The isotopologue order was $C^{18}O$, $^{13}CO$, $^{12}CO$, with a further breakdown via rotational transition, with $J = 3 - 2$, then $J = 2 - 1$, and finally $J = 1 - 0$. If multiple emission peaks are present in the spectrum, the strongest emission peak was chosen under the assumption that this would correspond to the highest column density along that line of sight (e.g. Urquhart et al. 2007, 2009; Eden et al. 2012, 2013). An example spectrum is displayed in Fig. 2, displaying the $^{13}CO\ J = 3 - 2$ line for the PGCC G224.34-2.00 from the CHIMPS2 survey (Eden et al. 2020; Eden et al., in preparation).

Using these surveys resulted in 273 of the 317 PGCCs having assigned velocities. The surveys used for each are listed in Table 1. The remaining 44 were assigned velocities using different methods. The first was to positionally cross-match the remaining sources with the ATLASGAL-survey catalogue, which contains velocities from a wide range of sources in the literature and a self-contained survey (full details can be found in Urquhart et al. 2018). This resulted in a further 16 allocated velocities. The remaining 28 velocities were assigned by extracting the spectra from the composite $^{12}CO\ J = 1 - 0$ survey of Dame et al. (2001). The data sets used from the composite survey are the first- and second-quadrant surveys of Dame et al. (2001), the survey of Cygnus X (Leung & Thaddeus 1992), and the third-quadrant survey of May et al. (1993).

The longitude-velocity ($\ell - V_{LSR}$) diagram of the PGCCs with a detected JPS (Eden et al. 2017) and/or SCOPE (Eden et al. 2019) source is displayed in Fig. 3. The sources are overlaid on the $^{12}CO\ J = 1 \rightarrow 0$ integrated emission from Dame et al. (2001). This emission traces the global Galactic distribution of molecular gas, and the PGCCs are well correlated with this emission. Also overlaid on the $^{12}CO\ J = 1 \rightarrow 0$ emission map are the loci of the spiral arms from Reid et al. (2019). The PGCCs are also tightly correlated with the spiral arms. The Galactic distribution of the PGCCs, and their relation to Galactic structure will be addressed in Section 5.

# 4 DISTANCE DETERMINATION

Determining the heliocentric distance to the PGCCs, and the compact sources within their substructure, is vital to calculating many physical properties of the sources. We have employed a multistage process to assign distances to all 317 observed PGCCs and, therefore, the 3178 associated compact sources. The steps in this process are outlined in Section 4.1, with the summary of distances assigned displayed in Table 2 and are in the order of reliability.

The velocities described in Section 3 are employed to determine kinematic distances to the majority of sources within this sample. However, sources within the Solar Circle (Galactocentric radius of $<8.15$ kpc; Reid et al. 2019) are subject to kinematic distance ambiguity (KDA), giving two potential distances to each source. Steps (iii)–(ix) in Section 4.1 relate to resolving this KDA, and assigning a unique distance to each source.

The rotation curve used to give Galactocentric radius ($R_{GC}$) measurements here is that of Brand & Blitz (1993). The choice of rotation curve is not vital, as available rotation curves agree within the errors in the distances (e.g. Eden et al. 2012), which are assumed to be of the order of 30 per cent (Duarte-Cabral et al. 2021).

## 4.1 Methodology

### 4.1.1 (i) Maser parallax

We matched the position of the PGCCs to the maser parallax catalogue of Reid et al. (2019), with a positional match (8 arcmin) in longitude, latitude, and velocity (km s$^{-1}$) allowing this distance to be adopted. This method resulted in distances to 6 PGCCs, with a total of 99 compact sources.

### 4.1.2 (ii) Outer Galaxy sources

Sources located at Galactocentric radii greater than 8.15 kpc have no KDA, and therefore the kinematic distance can be assigned. 79 PGCCs were assigned distances using this method, associated with 422 compact sources.

### 4.1.3 (iii) Tangent velocity

The KDA gives two equally spaced distance solutions about a tangent point. Those sources whose $V_{LSR}$ is within 10 km s$^{-1}$ of the tangent velocity are assigned the tangent distance. The two KDA solutions in this situation are closer together than any uncertainties associated with the distance-determination process (30 per cent; Duarte-Cabral et al. 2021). A total of 18 PGCCs, with 141 compact sources, were assigned distances using this method.

### 4.1.4 (iv) Scale height distribution

Studies have shown that high-mass star-forming regions are found towards the Galactic mid-plane, with a scale height of 30 pc (e.g. Reed 2000). We have set a tolerance for the scale height of the far-distance solution of four times this, 120 pc, following previous studies (e.g. Urquhart et al. 2011, 2018). If the far kinematic distance solution of a PGCC results in a projected scale height that is larger than this tolerance, it is placed at the near distance solution. This accounts for 54 and 493 PGCCs and compact sources, respectively.

### 4.1.5 (v) ATLASGAL comparisons

The remaining 160 sources were compared to the catalogue of the ATLASGAL survey, and their associated distances and velocities (Urquhart et al. 2018). These sources were matched positionally (8 arcmin tolerance), and any PGCCs that had a matching velocity within 10 km s$^{-1}$ had the ATLASGAL distance assigned to it. This method allowed for 79 PGCCs to be given distances, with an associated 1187 compact sources.

### 4.1.6 (vi) H I self-absorption, near distance

The HISA, H I self-absorption, method (e.g. Roman-Duval et al. 2009) compares the spectrum of H I emission to the radial velocity measured for a given source. If at the near distance, an absorption feature would be present in the H I spectrum as the cold H I embedded in a molecular cloud would absorb the emission from the warmer, background H I that is ubiquitous in the interstellar medium. This absorption feature would be coincident with the velocity measured for the PGCC. We compared the H I data from the Very Large Array Galactic Plane Survey (Stil et al. 2006) and the Galactic All-Sky Survey (McClure-Griffiths et al. 2009; Kalberla et al. 2010), and found absorption features coincident with the measured velocities of
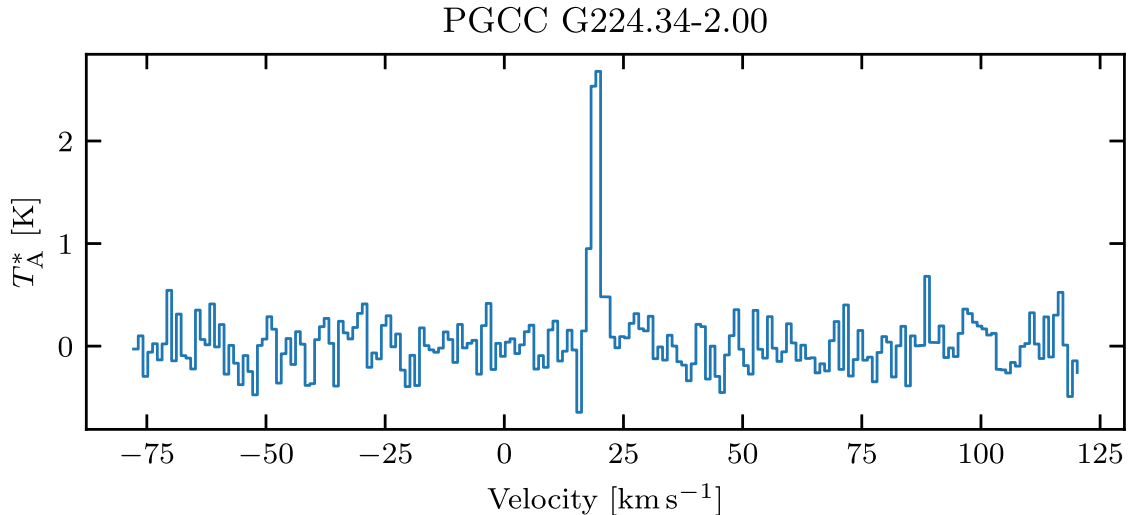
**Figure 2.** Example spectrum for velocity determination. This spectrum is for PGCC G224.34-2.00 and is the $^{13}$CO $J = 3 - 2$ line from the CHIMPS2 survey (Eden et al., in preparation). The velocity determined for this source was 19.3 km s$^{-1}$.

**Table 1.** Surveys used to assign radial velocities to the 317 PGCCs.

| Survey | Total | JPS PGCCs | SCOPE PGCCs | Molecular PGCCs | References transition |
|---|---|---|---|---|---|
| CHIMPS | 17 | 7 | 10 | $^{13}$CO/C$^{18}$O ($J = 3 - 2$) | [1] Rigby et al. 2016 |
| CHIMPS2 | 3 | 0 | 3 | $^{12}$CO/$^{13}$CO/C$^{18}$O ($J = 3 - 2$) | [2] Eden et al. 2020 |
| COHRS | 67 | 34 | 33 | $^{12}$CO ($J = 3 - 2$) | [3] Park et al. 2023 |
| SEDIGISM | 8 | 6 | 2 | $^{13}$CO/C$^{18}$O ($J = 2 - 1$) | [4] Schuller et al. 2021 |
| GRS | 27 | 20 | 7 | $^{13}$CO ($J = 1 - 0$) | [5] Jackson et al. 2006 |
| FUGIN | 89 | 52 | 37 | $^{12}$CO/$^{13}$CO/C$^{18}$O ($J = 1 - 0$) | [6] Umemoto et al. 2017 |
| MWISP | 62 | 0 | 62 | $^{12}$CO/$^{13}$CO/C$^{18}$O ($J = 1 - 0$) | [7] Su et al. 2019 |
| ATLASGAL | 16 | 13 | 3 | $^{13}$CO/C$^{18}$O ($J = 2 - 1$) | [8] Urquhart et al. 2018 |
| DHT Survey | 23 | 16 | 7 | $^{12}$CO ($J = 1 - 0$) | [9] Dame et al. 2001 |
| Cygnus X | 4 | 0 | 4 | $^{12}$CO ($J = 1 - 0$) | [10] Leung & Thaddeus 1992 |
| Third Quadrant | 1 | 0 | 1 | $^{12}$CO ($J = 1 - 0$) | [11] May et al. 1993 |

34 PGCCs, placing them at the near distance. These 34 PGCCs have 379 compact sources associated with them.

### 4.1.7 (vii) HISA far distance

Of the 47 PGCCs that did not have an absorption feature present in the H I, the remaining spectra had two potential solutions. The first is that the PGCC velocity was coincident with a peak in the H I spectrum. This is because the embedded H I is behind the background emission, and therefore, there is no absorption. The second was that it was an ambiguous feature, with a full explanation of this sort of feature found in Urquhart et al. (2018) and Duarte-Cabral et al. (2021). Seven PGCCs were assigned to the far distance, with 47 compact sources given those distances.

### 4.1.8 (viii) IRDC comparisons

The existence of an infrared dark cloud (IRDC) against the background infrared emission implies that a source is in the foreground, or at the near distance. A study of IRDCs found that 89 per cent were found to be at the near distance (Giannetti et al. 2015), therefore, if the PGCCs were coincident with an IRDC, we have placed them at the near distance. We positionally matched the remaining PGCCs without assigned distances to the IRDC catalogue of Peretto & Fuller (2009), within 8 arcmin, and found 25 that could be placed at the near distance. This also accounted for 291 compact sources.

### 4.1.9 (ix) Bayesian distance

A total of 15 PGCCs, and 119 compact sources, were left without distance assignment. We used the Bayesian distance model of Reid et al. (2016, 2019) which uses the positions of the spiral arms, derived from the maser parallaxes. This model preferentially places sources in the spiral arms, which is why it is not used to derive the distance for all PGCCs in this study. However, when all other available methods have been exhausted, we use this method.

### 4.2 Distance summary

We have derived distances to the 317 PGCCs, and therefore 3178 compact sources, from the SCOPE and JPS surveys within the Galactic Plane. These distances were assigned using the nine steps listed above. A tenth method was also used between steps (v) and (vi), comparing H I absorption features towards H II regions and comparisons to the H II region catalogues of Kolpak et al. (2003), Anderson & Bania (2009), and Urquhart et al. (2012) resulted in no assigned distances. The H II region catalogues of Urquhart et al. (2013) and Wienen et al. (2015) were not used as they were based on ATLASGAL data, and these distances would be accounted for in step 5. A small portion of the velocities, distances, and methods used for the individual PGCCs are displayed in Table 3. The full table is available from the Supporting Information. From this point forward, the compact sources JPS and SCOPE will be treated as one sample.
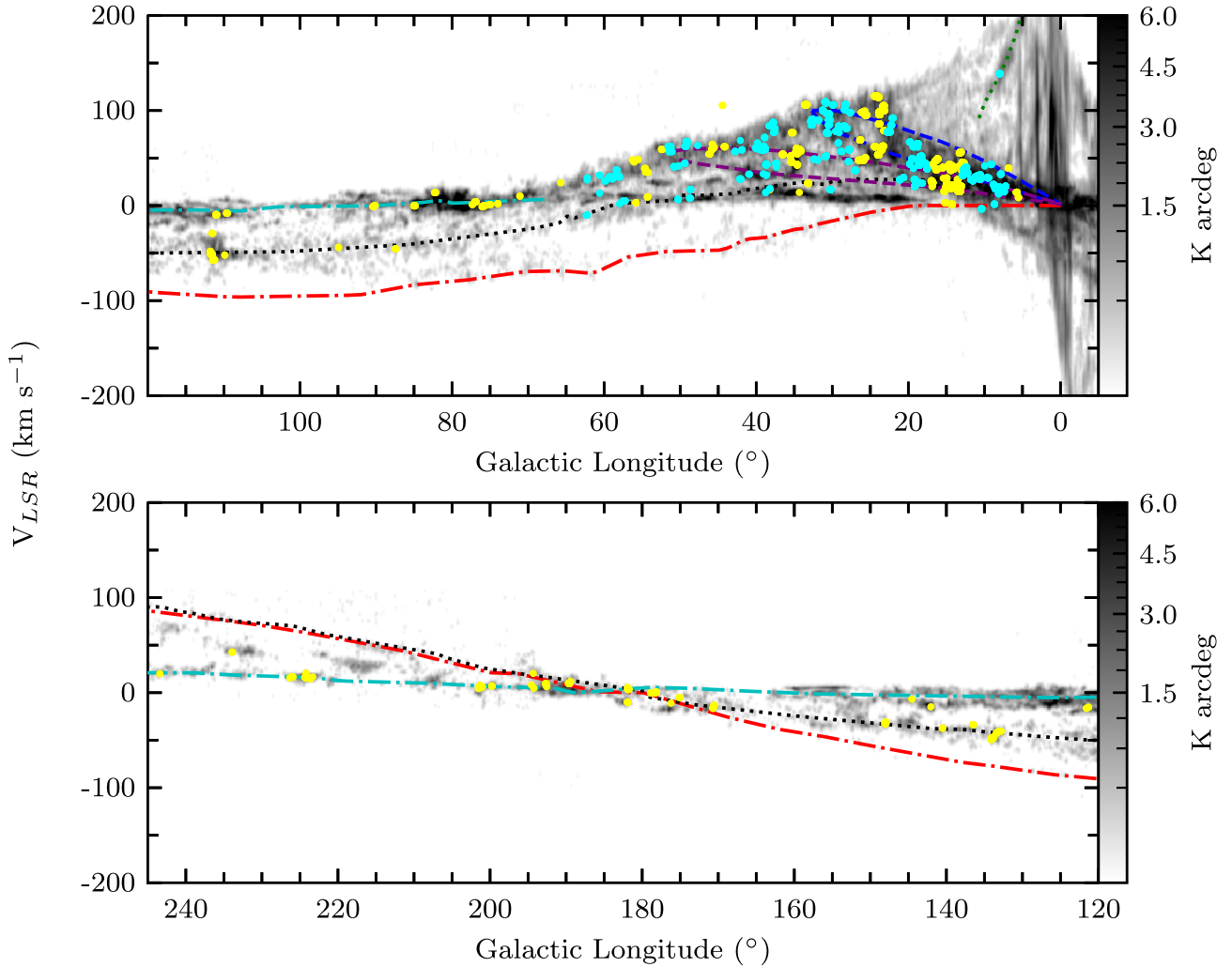
**Figure 3.** Longitude-velocity distribution of the PGCCs with detected JPS (cyan; Eden et al. 2017) and SCOPE (yellow; Eden et al. 2019) compact sources. The sources are plotted on top of the $^{12}CO\ J = 1 \to 0$ emission from the Dame et al. (2001) survey. The loci of the spiral arms from Reid et al. (2019) are also plotted. The Scutum–Centaurus Arm is the blue dashed line, the Sagittarius Arm is represented by the purple dashed line, the Perseus arm is the black dotted line, the red dot-dash line is the Outer Arm and the cyan dashed line is the Local Arm. The Connecting Arm is also displayed by the green dotted line.

**Table 2.** Summary of methods used to assign distances, with the number of PGCCs and compact sources determined at each step. The roman numerals in the first column relate to the steps detailed in Section 4.1.

| Step | Method | No. of PGCCs assigned | Associated compact sources |
|------|--------|------------------------|-----------------------------|
| (i) | Maser parallax | 6 | 99 |
| (ii) | Outer Galaxy | 79 | 422 |
| (iii) | Tangent velocity | 18 | 141 |
| (iv) | Scale height | 54 | 493 |
| (v) | ATLASGAL match | 79 | 1187 |
| (vi) | H I SA Near | 34 | 379 |
| (vii) | H I SA Far | 7 | 47 |
| (viii) | IRDC | 25 | 291 |
| (ix) | Bayesian method | 15 | 119 |

The distribution of the 317 PGCCs with derived distances is shown in Fig. 4. We have also positionally matched the PGCC sources not derived using method *(v)* above with compact sources from the ATLASGAL survey (Urquhart et al. 2018) in order to compare distance determinations. This comparison is shown in Fig. 5. There are 115 matches within an 8-arcmin search radius, with 88 (77 per cent) of these having a distance that can be considered to be consistent, i.e. within 1 kpc. 22 of the remaining 27 sources have the ATLASGAL source placed at a larger distance to that of the PGCC. However, although impacting the derived quantities of radius, mass, and mass surface density of individual sources, incorrect distance assignments are unlikely to affect ensemble properties (Rani et al. 2023).

## 5 GALACTIC DISTRIBUTION

In Figs 3 and 4, we show the results of the velocity and distance analysis presented in the previous sections. The positions of the

**Table 3.** Distance and velocity information for the PGCCs. The number in the $V_{LSR}$ reference column relates to the numbers in the reference column of Table 1, whilst the Distance Method column relates to the steps in Table 2.

| PGCC/Region | $V_{LSR}$ (km s$^{-1}$) | $V_{LSR}$ Reference | $R_{GC}$ (kpc) | Distance (kpc) | Distance Method |
|---|---|---|---|---|---|
| G28.38+0.10 | 105.4 | 3 | 4.2 | 5.7 | (viii) |
| G28.48+0.21 | 100.0 | 3 | 4.3 | 5.8 | (v) |
| G28.56−0.24 | 82.5 | 3 | 4.7 | 4.7 | (v) |
| G28.94−0.04 | 56.0 | 3 | 5.5 | 3.4 | (vi) |
| G29.18+0.24 | 76.0 | 3 | 4.9 | 4.3 | (viii) |
| G29.25−0.71 | 82.4 | 6 | 4.7 | 4.5 | (v) |
| G29.28−0.77 | 64.8 | 6 | 5.2 | 3.8 | (iv) |
| G29.31+0.17 | 81.0 | 3 | 4.8 | 4.5 | (vi) |
| G29.60−0.62 | 77.1 | 6 | 4.9 | 4.4 | (v) |
| G30.02−0.27 | 104.9 | 1 | 4.3 | 7.6 | (v) |
| G30.34+0.48 | 15.9 | 6 | 7.3 | 13.2 | (v) |
| G30.48+0.56 | 90.1 | 6 | 4.6 | 5.0 | (viii) |
| G30.52−0.11 | 89.2 | 1 | 4.6 | 4.9 | (vi) |
| G30.52+0.99 | 95.3 | 6 | 4.5 | 5.3 | (iv) |
| G30.55+0.16 | 83.6 | 6 | 4.8 | 5.0 | (ix) |

*Note.* Only a small portion of the data are displayed here, with the full table available from the Supporting Information.

sources are well correlated with the $^{12}$CO emission, as well as the spiral arms from the Reid et al. (2019) model. The correlation with the spiral arms is also clear from the face-on image of the Galaxy in Fig. 4.

Fig. 3 is split into two segments, the first covers $\ell = -5°$ to 120° and includes the four major spiral arms, the Scutum–Centaurus, Sagittarius, Perseus, and Outer arms. It also includes the Local Arm and the Connecting Arm. The Connecting Arm is thought to be the nearside dust lane around the Central Molecular Zone (CMZ) that are signs of accretion on to the CMZ (Sormani & Barnes 2019). The Connecting Arm appears to have one source associated with it, whilst the majority of the other sources can be found in the inner 30° of the Galaxy and associated with the Scutum–Centaurus and Sagittarius arms. There are also a significant number of sources found in the $\ell - V_{LSR}$ space between these two arms, a region where a connecting spur is identified (Stark & Lee 2006; Rigby et al. 2016). The Outer Arm does not appear to have any sources associated with it, away from the central 10° of the Galaxy, although the distance to the Outer Arm in this line of sight is large, which may lead to an observational bias.

In the second segment, covering $\ell = 120°$ to 240°, three spiral arms are found, the Perseus, Outer, and Local arms. Again in this segment, the spiral arms trace the positions of the PGCCs well. The $\ell - V_{LSR}$ spaces occupied by the Perseus and Outer arms are indistinguishable at longitudes greater than $\ell = 180°$. However, referring to the derived distances of the sources that occupy that $\ell - V_{LSR}$ space, two sources are found to be in the Outer Arm, as can be seen in Fig. 4.

The distribution of the PGCCs, and the associated compact sources, as a function of Galactocentric and heliocentric distance are displayed in Fig. 6. These two distributions reflect what is displayed in Figs 3 and 4, with a peak in the Galactocentric radii distribution found between 4 and 7 kpc, corresponding to the collection of sources found in the Scutum–Centaurus and Sagittarius arms. Further, smaller peaks are found at 8 and 12 kpc, which can be assigned to the first and second Galactic quadrant portions of the Perseus Arm, respectively. The heliocentric distances display a peak at approximately 3.5 kpc, which includes sources both in the Inner Galaxy and in the Perseus arm in the Galactic anticentre. There are also a significant number of sources found at distances of $\sim 5$ kpc,

corresponding to the Scutum–Centaurus and Sagittarius arms in the Inner Galaxy.

By using the spiral arm loci in $\ell - V_{LSR}$ space from Reid et al. (2019) and the derived Galactocentric distances, we determined the nearest spiral arms to each PGCC. If within 10 km s$^{-1}$, the PGCC is assumed to be associated with that arm. However, any PGCCs found to be more than 10 km s$^{-1}$ away from any spiral arm are considered to be interarm sources. This velocity cut is used as 95 per cent of SEDIGISM clouds are found to be within this tolerance of the nearest spiral arm (Urquhart et al. 2021).

# 6 PHYSICAL PROPERTIES

We calculate a series of physical properties for the compact sources, using the distances derived above and the flux information from the catalogues in Eden et al. (2017, 2019). For those sources with positionally matched ATLASGAL sources, the ATLASGAL temperatures are used. All other sources follow the distribution of temperatures as a function of Galactocentric radius in the ATLAS-GAL survey (Urquhart et al. 2018). A small portion of the calculated physical properties for the compact sources are contained in Table 4 with the full table available from the Supporting Information.

## 6.1 Masses

The JCMT compact source masses are calculated using the optically thin conversion:

$$M_{clump} = \frac{S_\nu D^2}{\kappa_\nu B_\nu(T_d)}, \tag{1}$$

where $S_\nu$ is the 850-µm integrated flux density, $D$ is the distance to the source, $\kappa_\nu$ is the mass absorption coefficient taken to be 0.01 cm$^2$ g$^{-1}$, whilst also accounting for the gas-to-dust ratio of 100 (Mitchell et al. 2001); and $B_\nu(T_d)$ is the Planck function evaluated at $T_d$, where $T_d$ is the temperature derived from the matching ATLASGAL source or the fit of average clump temperatures as a function of Galactocentric radius from figure 12 in Urquhart et al. (2018), with a median temperature of 19.8 K.

The distribution of masses of the compact sources is displayed in Fig. 7. The plotted quantity is the bin population per unit mass interval, $\Delta N/\Delta M$, with the histogram of the entire catalogue using equal bin widths shown in grey. The superimposed points show the mass distributions using equal bin populations, to equalize the weights from Poisson errors (Maíz Apellániz & Úbeda 2005). These are separated into the entire catalogue, the sources associated with individual spiral arms and the interarm sources. The last point positions are calculated as in Eden et al. (2015, 2018), with the mass coordinate represented by the median value in each bin.

By assuming a power-law slope of the form $\Delta N/\Delta M \propto M^\alpha$, a least-squares fit can be applied above the completeness limits to calculate the values of the indices, $\alpha$. The completeness limits were determined as the most-massive bin that follows two bins of lower $\Delta N/\Delta M$ values, or in the case of the Outer arm, which does not fit this criterion, the highest value of $\Delta N/\Delta M$. The least-squares fit uses an outlier-resistant method to ensure that the last bin, which is potentially quite wide, does not influence the fit unduly (Eden et al. 2018). The values for the indices, and the corresponding completeness limits (the lower end of the fitting range) are given in Table 5.

The index values for the individual spiral arms are all consistent within 3σ with the total sample, except for the Sagittarius arm and the Interarm regions, which are steeper by more than $\sim 5$σ. The Sagittarius Arm has been postulated as being different
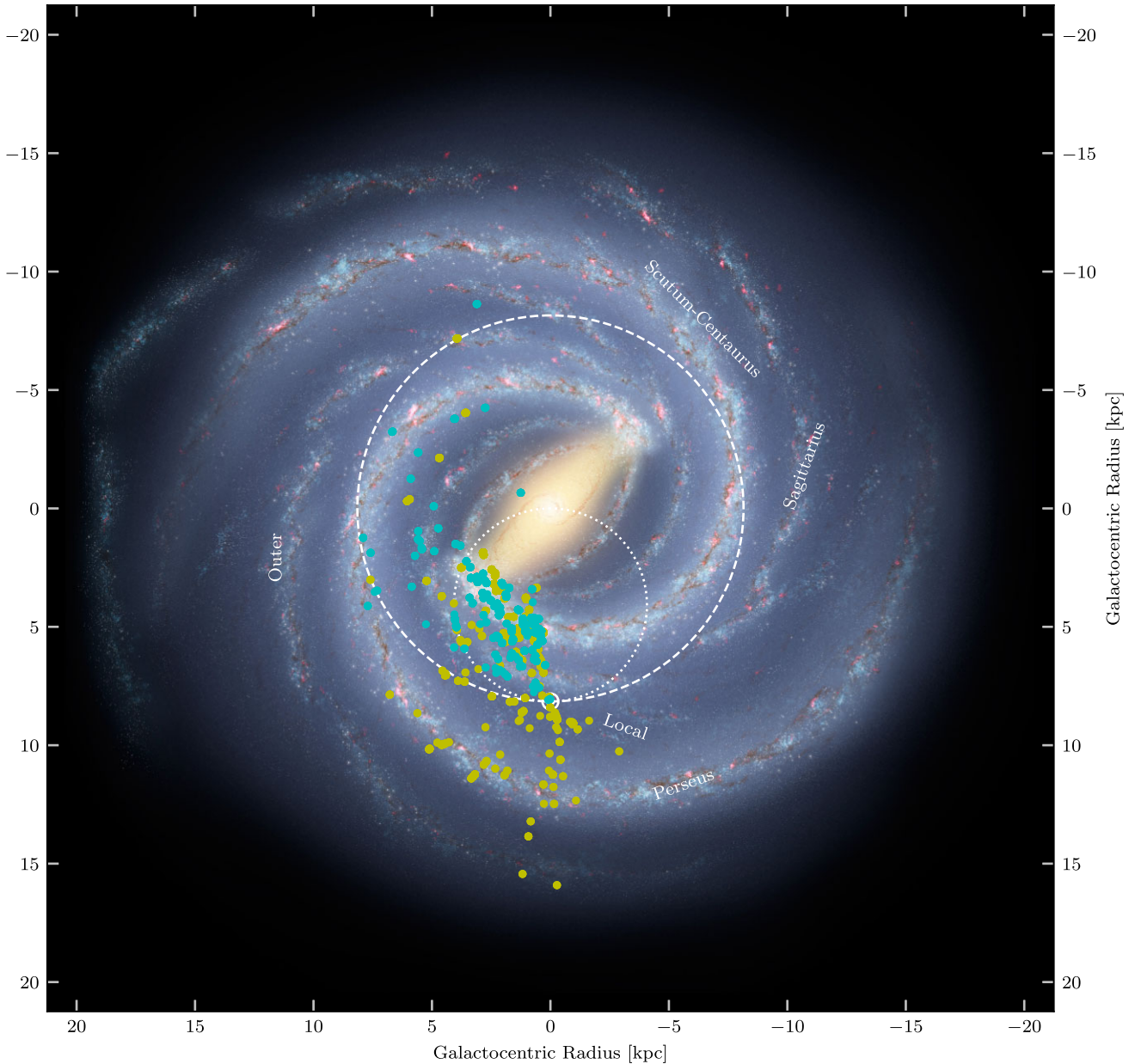
**Figure 4.** Face-on view of the distribution of the 317 PGCCs (JPS in cyan, SCOPE in yellow) using the kinematic distances derived here. They are overlaid on the schematic of the Milky Way produced by Robert Hurt of the Spitzer Science Center, in consultation with Robert Benjamin (University of Wisconsin–Whitewater). The position of the Sun is indicated by the white solar symbol, with the white dotted line representing the tangent positions and the white dashed line showing the extent of the Solar Circle. We have also indicated the positions of the four major spiral arms, and the Local Arm.

from the two 'major' spiral arms: Perseus and Scutum–Centaurus (Benjamin 2008). However, it is unclear if this would be reflected in the clump-mass function, since there is no evidence of a difference in its star-formation properties (Urquhart et al. 2014a).

The physics of the interarm regions may influence the steeper index found for these clumps. Modelling indicates molecular clouds within a spiral potential are more massive (Dobbs, Burkert & Pringle 2011). Observations and simulations have indicated that there is a statistical link between the stellar initial mass function and clump-mass distributions (e.g. Simpson, Nutter & Ward-Thompson 2008; Pelkonen et al. 2021) with an altered initial mass function found

(IMF) in more-massive clouds (Weidner, Kroupa & Bonnell 2010). This altered IMF tends to be more top-heavy, i.e. flatter, and is caused by the suppression of fragmentation due to radiative feedback (Krumholz, Klein & McKee 2011), which reflects the conditions found in spiral arms compared with interarm regions (Koda et al. 2012). The excitation temperatures, linewidths, and virial parameters of interarm clouds are also found to be lower in the interarm regions (Rigby et al. 2019). This is taken to be a result of the lack of external pressure that is applied from the ambient arm material in the spiral arms, which allows the clouds with higher virial parameters to disperse in the interarm. This breakup of molecular clouds would allow for less opportunity for clumps to form.
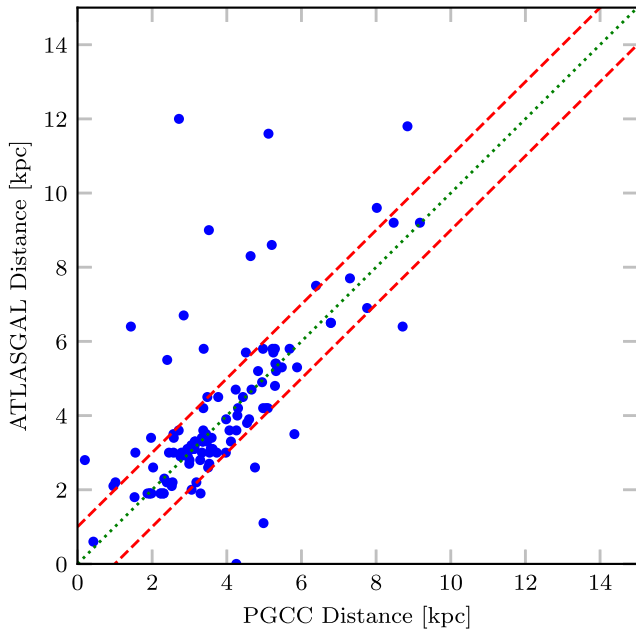
**Figure 5.** Distance comparison of PGCC sources in the JPS and SCOPE surveys with the compact sources of the ATLASGAL survey (Urquhart et al. 2018). The green dotted line represents the 1:1 line, whereas the red dashed lines are the 1 kpc limits.

Along with power-law fits, mass functions have also been found to be well described by lognormal distributions (e.g. Peretto & Fuller 2010; Wienen et al. 2015). We fit each sample, the total and the individual spiral arms, with an adapted version of the expression outlined in Peretto & Fuller (2010) in which the mass function has the form $\Delta N/\Delta M = Ae^{-x}$ where:

$$x = \frac{(\log_{10}M - \log_{10}M_{\text{peak}})^2}{2\sigma^2}. \tag{2}$$

In this form, $A$ is a constant, $M$ is the bin mass, $M_{\text{peak}}$ is the mass at the peak of the distribution, and $\sigma$ is the dispersion of the distribution. The values for $M_{\text{peak}}$ and $\sigma$ are presented in Table 5, with the fits displayed in the lower panel of Fig. 7. No value is presented for the Outer Arm as a lognormal fit did not converge for that sample. The completeness limits and values for $M_{\text{peak}}$ are in good agreement for the Scutum–Centaurus and Sagittarius arms, along with the interarm sample. The remaining distributions, the total sample, and Perseus and Local arms have $M_{\text{peak}}$ values below the inferred completeness limit, indicating the peaks are not well constrained. However, for all samples, other than the aforementioned Outer Arm distribution, they are better described as lognormal as opposed to power-law fits, as indicated by the $\chi^2$ values for each fit, as shown in Table 5.

### 6.2 Radii, column, and surface densities

The cumulative distributions of the compact source radii, column densities, and surface densities are shown in the top, middle, and bottom panels of Fig. 8, respectively. These distributions are split into sources associated with the individual spiral arms.

The radii were calculated using the effective radii of the compact sources, as reported in Eden et al. (2017, 2019) and the distances calculated above.

The column densities were calculated using the following equation:

$$N_{\text{H}_2} = \frac{S_{\nu,\text{peak}}}{B_\nu(T_{\text{d}})\Omega_{\text{b}}\kappa_\nu m_{\text{H}}\mu}, \tag{3}$$

where $B_\nu(T_{\text{d}})$ and $\kappa_\nu$ are as defined in the previous section, $\Omega_{\text{b}}$ is the solid angle of the beam from a full width at half-maximum of 14.4 arcsec (Eden et al. 2017), $m_{\text{H}}$ is the mass of a hydrogen atom, and $\mu$ is the mean mass per hydrogen molecule, taken to be 2.8 (Kauffmann et al. 2008). $S_{\nu,\text{peak}}$ is the peak flux density, where the SCOPE fluxes are converted from mJy arcsec$^{-2}$ to Jy beam$^{-1}$. The mass surface densities ($M_{\text{clump}}/\pi R^2$) make use of the masses and radii for each compact source.

The statistics of these distributions are shown in Table 6, with the values for individual compact sources presented in Table 4. The column density and mass surface densities are largely consistent with each other, which is not unsurprising since these quantities are fairly insensitive to heliocentric distance (Dunham et al. 2011). However, differences in the mass surface density of molecular clouds are found between spiral arms and interarm environments (Colombo et al. 2022). Since these differences are not reflected in the compact sources formed within these molecular clouds, it is more evidence to support conclusions drawn from Galactic Plane studies, that once a compact source forms within a molecular cloud, the environment in which it resides has very little impact on its properties (e.g. Eden et al. 2013; Urquhart et al. 2015, 2018, 2022), since no environmental variations are found. The column densities have statistics similar to those found from previous studies of SCUBA-2 PGCCs, with consistent mean values (e.g. Mannfors et al. 2021).

The mean radii of compact sources in each spiral arm are not statistically consistent with each other, with Anderson–Darling (A–D) tests finding that they are largely not drawn from the same sample. The Local and Outer arms are the biggest outliers (A–D $p$-values ≪ 0.001), with the radii of Local Arm sources significantly lower, and the Outer Arm sources larger. This is not surprising due to the heliocentric distances involved, and previous studies finding the classification of sources detected varying with distance (e.g. Dunham et al. 2011).

## 7 STAR FORMATION IN PGCCS

### 7.1 Prestellar and protostellar compact sources

Previous observations have found that the star formation in PGCCs is low compared with other star-forming regions in the Milky Way (e.g. Tang et al. 2018; Yi et al. 2018; Zhang et al. 2018). To determine if a compact source from the sample in this study is hosting a young stellar object, a positional match within 40-arcsec was made with the band-merged catalogue of the Hi-GAL survey (Elia et al. 2017, 2021), where the presence of a Hi-GAL band-merged source containing a 70-μm source indicated that it was protostellar following the methodology used in a number of studies (e.g. Ragan et al. 2016, 2018; Elia et al. 2017, 2021). This resulted in a sample of 2107 protostellar compact sources that will be used to calculate star-formation efficiencies in Section 7.4 using their Hi-GAL-determined luminosity (Elia et al. 2017, 2021). The luminosities were scaled using the Hi-GAL-derived distances (Mège et al. 2021) and the distances in this study. As a result of this matching, a total of 1071 prestellar compact sources were identified.
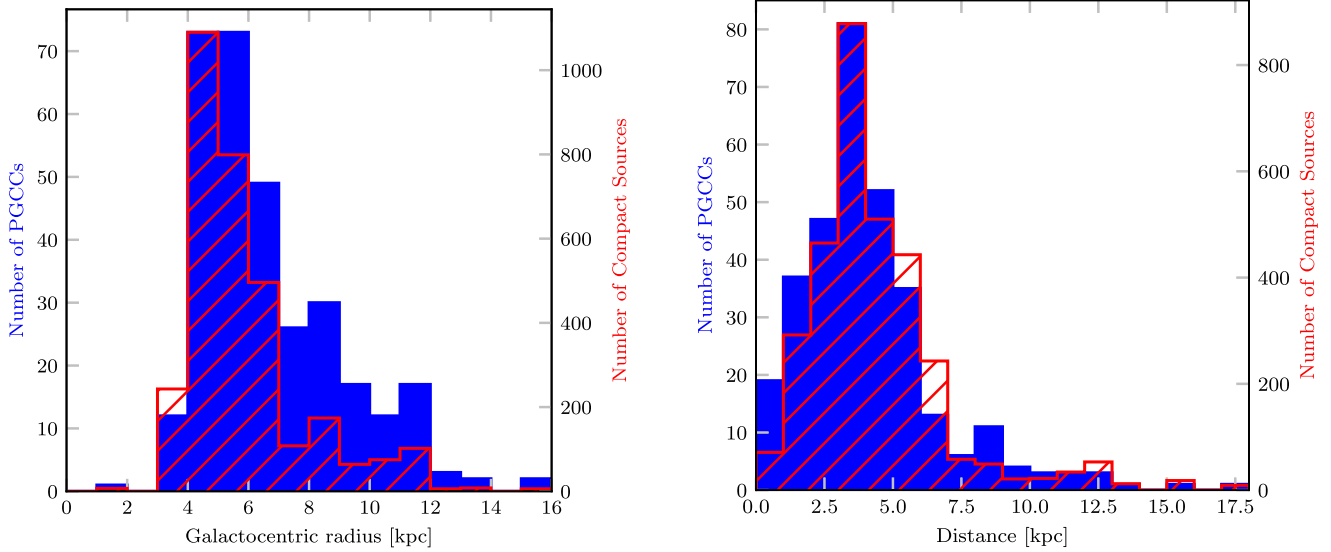
**Figure 6.** Distribution of PGCCs (blue, solid histogram) and the associated compact sources (red, hashed histogram) as a function of Galactocentric radius and heliocentric distance in the left and right panels, respectively.

**Table 4.** Derived compact-source parameters.

| Source name | Region | $\ell_{peak}$ (°) | $b_{peak}$ (°) | $V_{LSR}$ (km s$^{-1}$) | Distance (kpc) | Radius (pc) | log[$N_{H_2}$] (cm$^{-2}$) | log[Mass surface density] (M$_\odot$ pc$^{-2}$) | log[$M_{clump}$] (M$_\odot$) |
|---|---|---|---|---|---|---|---|---|---|
| SCOPEG005.83−00.94 | G005.91−01.00 | 5.831 | −0.935 | 13.0 | 2.95 | 0.37 | 22.901 | 3.018 | 2.657 |
| SCOPEG005.84−01.00 | G005.91−01.00 | 5.838 | −0.995 | 13.0 | 2.95 | 0.93 | 23.045 | 2.866 | 3.301 |
| SCOPEG005.85−00.99 | G005.91−01.00 | 5.853 | −0.993 | 13.0 | 2.95 | 0.50 | 22.893 | 2.960 | 2.857 |
| SCOPEG005.87−00.99 | G005.91−01.00 | 5.873 | −0.994 | 13.0 | 2.95 | 0.57 | 22.757 | 2.875 | 2.888 |
| SCOPEG005.88−00.94 | G005.91−01.00 | 5.879 | −0.943 | 13.0 | 2.95 | 0.83 | 22.683 | 2.790 | 3.127 |
| SCOPEG005.89−00.91 | G005.91−01.00 | 5.885 | −0.914 | 13.0 | 2.95 | 0.56 | 22.543 | 2.712 | 2.704 |
| SCOPEG005.89−00.94 | G005.91−01.00 | 5.892 | −0.944 | 13.0 | 2.95 | 0.46 | 22.923 | 2.879 | 2.698 |
| SCOPEG005.90−00.93 | G005.91−01.00 | 5.904 | −0.931 | 13.0 | 2.95 | 0.44 | 22.749 | 2.797 | 2.589 |
| SCOPEG005.91−00.95 | G005.91−01.00 | 5.914 | −0.951 | 13.0 | 2.95 | 0.73 | 23.143 | 2.889 | 3.113 |
| SCOPEG005.92−00.99 | G005.91−01.00 | 5.917 | −0.990 | 13.0 | 2.95 | 0.89 | 23.072 | 2.994 | 3.388 |
| SCOPEG005.92−00.96 | G005.91−01.00 | 5.923 | −0.955 | 13.0 | 2.95 | 0.32 | 22.543 | 2.714 | 2.207 |
| SCOPEG005.92−00.97 | G005.91−01.00 | 5.924 | −0.967 | 13.0 | 2.95 | 0.42 | 22.526 | 2.676 | 2.410 |
| SCOPEG006.91+00.88 | G006.9+00.8A1 | 6.914 | 0.879 | 38.4 | 4.84 | 0.80 | 22.373 | 2.535 | 2.836 |
| SCOPEG006.94+00.91 | G006.9+00.8A1 | 6.940 | 0.910 | 38.4 | 4.84 | 0.54 | 22.547 | 2.829 | 2.789 |
| SCOPEG006.94+00.92 | G006.9+00.8A1 | 6.940 | 0.921 | 38.4 | 4.84 | 1.27 | 22.539 | 2.637 | 3.339 |

*Note.* Only a small portion of the catalogue is shown here. The entire catalogue is available in the Supporting Information.

### 7.2 Properties of proto- and prestellar compact sources

We can now compare the physical properties derived in Section 6 for the protostellar and prestellar compact source subsamples.

The mass functions are displayed in Fig. 9. The indices of the protostellar and prestellar mass functions are found to be $\alpha = -1.16 \pm 0.04$ and $\alpha = -1.28 \pm 0.05$, respectively. These indices and peak values are consistent with each other, a result not matching that of the Hi-GAL survey (Elia et al. 2017). The mass ranges of the two samples are also consistent, something also not observed in Hi-GAL (Elia et al. 2017). It is, however, consistent with a previous PGCC result in Mannfors et al. (2021). The improved angular resolution of the JCMT compared with *Herschel* may be the cause of this, something speculated on by Elia et al. (2017). The mass functions presented here are also not split by distance, and are averaged over all Galactic environments, whereas the Hi-GAL study

split their mass functions into 0.5 kpc heliocentric distance bins. By combining multiple distances here, we may have averaged out these differences. As with the mass distributions of the individual spiral arms, we also fit lognormal distributions to the mass functions. The $\chi^2$ values for the power-law fits were found to be 28.87 and 25.01 for the protostellar and prestellar mass functions, respectively, whilst for the lognormal fits were 2.94 and 2.97, respectively. As with the earlier mass distributions, these samples are best described by a lognormal distribution.

The cumulative distributions of the radii, column densities, and surface densities for the protostellar and prestellar subsamples are displayed in Fig. 10. A–D tests were performed on each set and these found that the null hypothesis that the radii and column densities of protostellar and prestellar clumps are drawn from the same population can be rejected at a probability of ≪0.001. Whereas
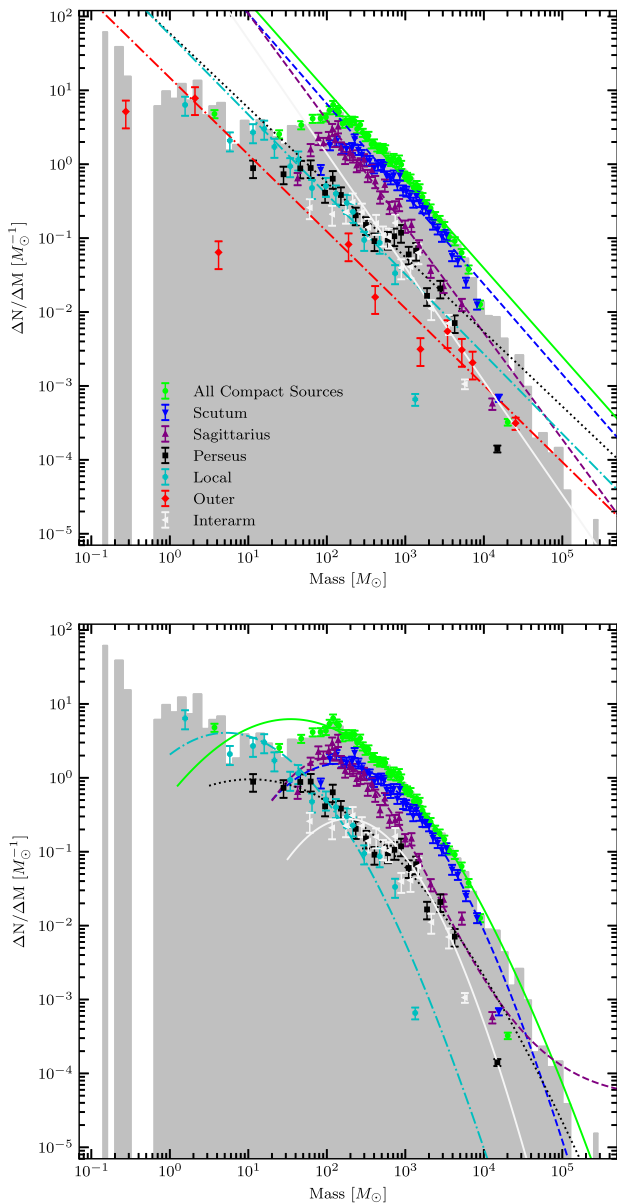
**Figure 7.** The clump-mass distributions of all the compact sources in the Galactic Plane PGCCs, along with the mass distributions of the different spiral arms. The grey histogram is the entire compact source catalogue. The points represent the mass distributions as described in the text, using equally populated bins. The green circles are for the entire catalogue, the downwards-pointing blue triangles are the Scutum–Centaurus Arm, the upwards-pointing purple triangles are the Sagittarius Arm, the black squares are the Perseus Arm, the cyan circles are the Local Arm, with the red diamond and left white triangles representing the Outer Arm and Interarm sources, respectively. The fits for the total sample, Scutum–Centaurus, Sagittarius, Perseus, Local, Outer arms, and Interarm are indicated by the solid green, dashed blue, dashed purple, dotted black, dot–dash cyan, dot–dash red, and white solid lines, respectively. The top panel displays the least-squares fits to these distributions, assuming the form of a power law, whilst the bottom panel indicates lognormal fits to the distributions. The sample for the Outer Arm is omitted from the lognormal distributions since a fit was not possible to that sample.

this cannot be rejected in the mass surface densities, which found a A–D *p*-value of 0.028, or 2.2-σ. The ATLASGAL survey split their protostellar sample into 70-μm-bright, mid-IR bright, and massive star forming. Differences were found between prestellar and star-forming sources as traced by massive-star formation indicators (Urquhart et al. 2018), although when samples complete in mass and column density were used, their differences largely disappeared (Billington et al. 2019; Urquhart et al. 2022).

## 7.3 Mass–radius relationship

The relationship between the mass and size of a molecular cloud was initially described by Larson (1981) indicating that a constant column density, with respect to radius, was found. Further work found that different slopes were required to describe sources that are star forming, and within which mass regime that star formation was occurring (Kauffmann et al. 2010).

The mass–radius relationship for the SCOPE compact sources is displayed in Fig. 11. The sample is again split into protostellar and prestellar sources. Both subsamples show that these two parameters are well correlated, with Pearson correlation coefficients of 0.92 and 0.91, respectively. Linear least-squares fitting gives slopes of $2.089 \pm 0.019$ and $2.083 \pm 0.028$ for the protostellar and prestellar subsamples, respectively. This is consistent with the relationship found by the initial *Planck* PGCC analysis (Planck Collaboration XXVIII 2016), but it is steeper than the relationship found in the ATLASGAL survey of $1.647 \pm 0.012$ (Urquhart et al. 2018). The steepness of this relationship may point towards the more-quiescent nature of PGCCs, even in those that are forming stars. The slopes found here are consistent with the relationship found in quiescent molecular clouds in a tidal dwarf galaxy, whilst the ATLASGAL slope is consistent with the star-forming molecular clouds in that particular galaxy (Querejeta et al. 2021).

Fig. 11 is separated into three regions, each with a different significance. The green shaded area is where low-mass star formation would occur, whilst high-mass star formation would be expected to occur in the unshaded regions. This delineation is defined by the relationship $m(r) = 580\,\mathrm{M}_\odot (R_{\mathrm{eff}}/\mathrm{pc})^{1.33}$, below which would be mainly low-mass star formation (Kauffmann & Pillai 2010). The final region, indicated in yellow, is where young massive clusters would form (Bressert et al. 2012). The majority (88.5 per cent) of PGCC compact sources are found in the high-mass star-forming space, with this fraction identical in both prestellar and protostellar sources. Notably, no young massive cluster-forming sources ($M \gtrsim 10^4\,\mathrm{M}_\odot$, younger than 100 Myr; Portegies Zwart, McMillan & Gieles 2010) are found in this study, either protostellar or prestellar. It is not surprising that no starless examples were found, since numerous studies have also failed to find any in the Galactic disc (e.g. Ginsburg et al. 2012; Longmore et al. 2017; Urquhart et al. 2018).

There are a number of compact sources on the edge of the cluster-forming source region, namely SCOPEG015.01−00.67, SCOPEG035.58+00.05, SCOPEG077.46+01.76, and SCOPEG181.92+00.36. The first two, SCOPEG015.01−00.67 and SCOPEG035.58+00.05, are coincident with ATLASGAL sources, with the masses reported here higher and with smaller radii. We found the former to be prestellar, however, the ATLASGAL source is associated with a tracer of massive star formation. These sources close to the border of this region may move into, or further away from it, with a different temperature or distance assignment. However, as candidate young massive clusters, additional data are needed to confirm their nature.

**Table 5.** Fit parameters for the mass distributions of the entire compact-source sample, and those for the individual spiral arms. The indices of the power-law fits, the completeness limits, and therefore, the lower end of the fitting range for these indices are also shown. The lognormal peaks and dispersions are listed, along with the $\chi^2$ for each fit.

| Spiral arm | Index | Completeness limit ($M_\odot$) | $\chi^2$ Power law | $M_{peak}$ ($M_\odot$) | $\sigma$ (log[$M_\odot$]) | $\chi^2$ Lognormal |
|---|---|---|---|---|---|---|
| Total | $-1.20 \pm 0.03$ | 120 | 378.50 | 35 | 6.81 | 4.09 |
| Scutum–Centaurus | $-1.22 \pm 0.05$ | 220 | 249.76 | 140 | 4.88 | 1.48 |
| Sagittarius | $-1.44 \pm 0.04$ | 110 | 86.95 | 100 | 1.38 | 2.80 |
| Perseus | $-1.01 \pm 0.07$ | 60 | 56.84 | 11 | 8.36 | 1.79 |
| Local | $-1.08 \pm 0.05$ | 95 | 86.74 | 5.2 | 5.44 | 10.14 |
| Outer | $-1.04 \pm 0.06$ | 2.0 | 50.52 | | | |
| Interarm | $-1.54 \pm 0.15$ | 210 | 63.73 | 180 | 4.07 | 0.99 |

## 7.4 Star formation efficiency and *L/M*

### 7.4.1 L/M *in individual compact sources*

The luminosity-to-mass ratio (*L/M*) is often taken to be an analogue of the instantaneous star-formation efficiency (SFE; e.g. Molinari et al. 2008; Urquhart et al. 2014b; Eden et al. 2015; Liu et al. 2016), when the luminosity is taken from the embedded young stellar objects and the mass is that of the clump or cloud. This ratio is calculated for the entire star-forming sample and for the individual spiral-arm subsets of this, using the luminosities from Elia et al. (2017, 2021) and the masses calculated in Section 6.1. The cumulative distributions of *L/M* are displayed in Fig. 12, with the statistics displayed in Table 7.

The (sub)sample distributions are statistically consistent with each other. However, the mean *L/M*, or SFE, of the Outer spiral arm deviates slightly by ∼2σ from the other arms. The A–D tests demonstrate that the Scutum–Centaurus, Sagittarius, and Perseus samples were drawn from the same population, and that the null hypothesis that the Outer arm sources were drawn from the same population can be rejected. The Interarm and Local sources were found to have A–D test *p*-values of 0.209 and 0.029, respectively. The null hypothesis could not be rejected as these values correspond to 2.18σ and 1.25σ, respectively.

These values are significantly lower than those found in other Galactic Plane studies (Eden et al. 2015; Urquhart et al. 2018) and are more consistent with the *L/M* ratio found in quiescent clumps in the ATLASGAL survey, despite the presence of 70-µm sources. The values are also consistent with previous SCOPE determinations of *L/M* (Eden et al. 2019) of sources located both in and out of the Galactic Plane, with no evidence found to contradict prior results of low levels of star formation within PGCCs.

### 7.4.2 L/M *across the Galactic Plane*

The ratio *L/M* as a function of Galactocentric radius is shown in Fig. 13. This distribution shows the values of individual clumps (grey points) and the mean in each 0.5-kpc bin (blue points). As displayed in Fig. 13, there is a large variation in values of *L/M* from clump to clump. However, the 0.5-kpc averages show very little variation, with only three bins, at 1.75, 3.25, and 6.75 kpc, varying from the mean by greater than 5σ. These bins lie below the average, with those at 1.75 and 3.25 kpc containing 7 and 3 compact sources, respectively. The 6.75-kpc bin is consistent with results of Eden et al. (2015), who found a lowered *L/M* ratio at these Galactocentric radii, coincident with the interarm regions between the Sagittarius and Perseus arms.

The overall trend of no significant variation of the mean on kiloparsec scales is consistent with results from blind Galactic Plane surveys (Moore et al. 2012; Eden et al. 2015; Ragan et al. 2016, 2018; Urquhart et al. 2018). These studies found no significant increase in *L/M* that can be attributed to spiral arms, or other features of Galactic structure. Since there is more potentially star-forming material (including PGCCs) in the spiral arms, these studies have concluded that the spiral arms are collecting material, and not impacting the star-formation process.

The similarities to these studies, however, is only when looking at relative changes from bin to bin. The absolute values of *L/M* are much lower than those reported in similar studies (Eden et al. 2015; Urquhart et al. 2018), as mentioned in Section 7.4.1. The mean value of *L/M* in this work is $0.727 \, L_\odot/M_\odot$, which is almost an order of magnitude lower than those in the aforementioned studies ($1.17 \, L_\odot/M_\odot$ and $18.8 \, L_\odot/M_\odot$ for Eden et al. 2015 and Urquhart et al. 2018, respectively).

## 8 ARE PGCCS A DIFFERENT POPULATION?

The concentration of star-forming structures in the plane of the Milky Way makes it the ideal laboratory for determining if PGCCs are indeed a separate population. The previous sections have demonstrated that the physical and star-forming properties of PGCCs (mass, radius, column density, mass surface density, SFE) do not vary as a function of Galactic environment. As a result, we can assume that the whole PGCC catalogue (Planck Collaboration XXIII 2011, XXVIII 2016) can be taken as one population. We can then compare the ATLASGAL dust-continuum-traced clumps that are associated with a catalogued PGCC with those that are not associated with a PGCC, and determine if PGCCs are indeed a separate population.

Positional matching of the PGCC catalogue (Planck Collaboration XXIII 2011, XXVIII 2016) with the ATLASGAL catalogue (Urquhart et al. 2018) resulted in 2128 and 5473 associated and non-associated ATLASGAL-PGCC sources, respectively.

The ATLASGAL-derived properties of temperature, column density, and *L/M* of these two samples are compared as cumulative distributions in Fig. 14. These properties are chosen due to the cold, dense, low-star-forming nature of PGCCs (e.g. Planck Collaboration XXVIII 2016; Zhang et al. 2016, 2018). The distributions in Fig. 14 demonstrate that PGCC-ATLASGAL sources are indeed lower in star-formation efficiency, lower in temperature and denser, with A–D tests indicating that they are drawn from different populations (all *p*-values ≪0.001 that they are drawn from the same sample). Further to this, the previous section (Section 7.4.2) determined that the *L/M*
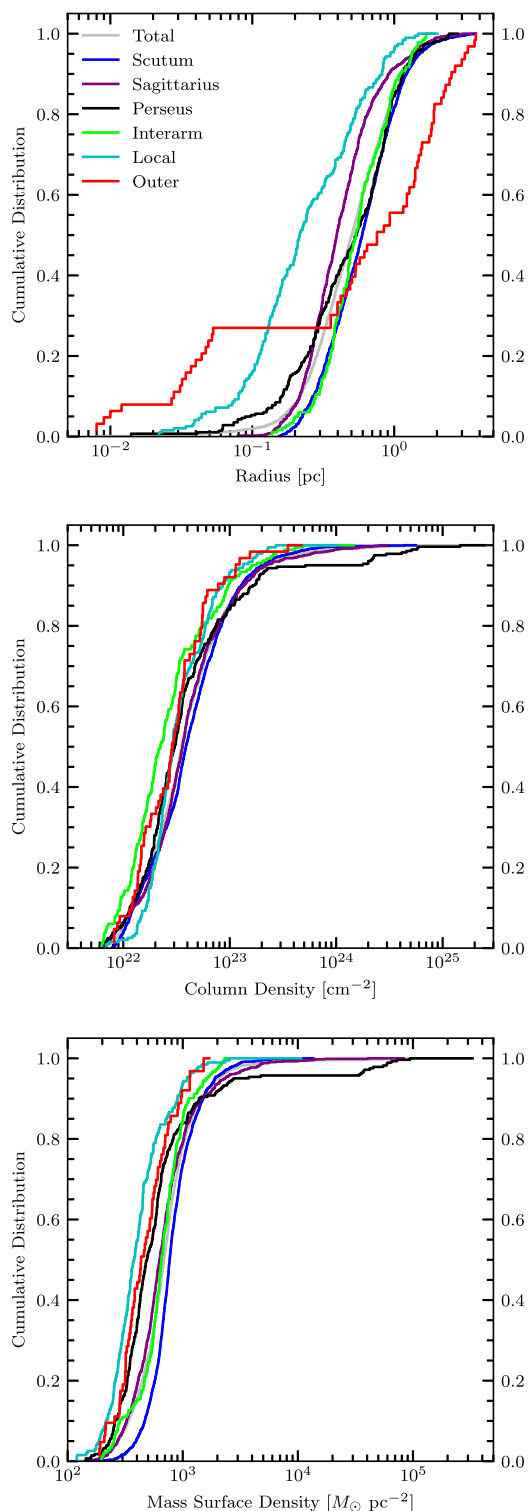
**Figure 8.** Cumulative distributions of compact source radii, peak column densities, and surface densities in the top, middle, and bottom panels, respectively. The total sample, Scutum–Centaurus, Sagittarius, Perseus, Local, Outer, and Interarm samples are represented by the grey, blue, purple, black, cyan, red, and lime lines, respectively.

**Table 6.** Statistics for physical parameters in the compact-source sample and the individual spiral-arm subsets. The mean ($\bar{x}$), standard error, standard deviation ($\sigma$), and median values are given. The first row in each section describes the entire sample.

| Parameter/Spiral arm | $\bar{x}$ | $\frac{\sigma}{\sqrt{N}}$ | $\sigma$ | Median |
|---|---|---|---|---|
| **Radius (pc)** | 0.63 | 0.01 | 0.47 | 0.50 |
| Scutum–Centaurus | 0.70 | 0.01 | 0.46 | 0.60 |
| Sagittarius | 0.51 | 0.01 | 0.40 | 0.39 |
| Perseus | 0.63 | 0.03 | 0.46 | 0.55 |
| Local | 0.34 | 0.02 | 0.31 | 0.22 |
| Outer | 1.15 | 0.13 | 1.07 | 0.85 |
| Interarm | 0.64 | 0.03 | 0.35 | 0.54 |
| **log[$N_{\rm H_2}$ (cm$^{-2}$)]** | 22.60 | 0.01 | 0.43 | 22.55 |
| Scutum–Centaurus | 22.62 | 0.01 | 0.40 | 22.09 |
| Sagittarius | 22.61 | 0.01 | 0.43 | 22.56 |
| Perseus | 22.61 | 0.04 | 0.59 | 22.49 |
| Local | 22.53 | 0.02 | 0.31 | 22.46 |
| Outer | 22.49 | 0.05 | 0.36 | 22.48 |
| Interarm | 22.44 | 0.03 | 0.42 | 22.35 |
| **log[Mass Surface Density (M$_\odot$ pc$^{-2}$)]** | 2.91 | 0.00 | 0.28 | 2.84 |
| Scutum–Centaurus | 2.91 | 0.01 | 0.21 | 2.89 |
| Sagittarius | 2.83 | 0.01 | 0.30 | 2.80 |
| Perseus | 2.79 | 0.03 | 0.44 | 2.69 |
| Local | 2.61 | 0.02 | 0.26 | 2.58 |
| Outer | 2.65 | 0.03 | 0.22 | 2.63 |
| Interarm | 2.82 | 0.02 | 0.22 | 2.82 |

ratio of PGCC-associated compact sources was lower than other Galactic Plane sources, consistent with ratios found for quiescent clumps (Urquhart et al. 2018)

## 9 SUMMARY AND CONCLUSIONS

We have investigated the physical properties of PGCCs within one degree of the Galactic Plane from the JPS and SCOPE surveys to determine whether PGCCs are a separate population of Galactic clumps.

Using a suite of molecular surveys, velocities, and distances were assigned to 317 PGCCs and 3178 compact sources, also allowing them to be attributed to a spiral arm. These distances were used to determine masses, radii, and mass surface densities for the compact sources, along with column densities.

The mass functions of both the total sample and individual spiral arms are, in general, better described as lognormal distributions as opposed to power laws. All spiral-arm distributions are consistent with each other, except for the Sagittarius Arm and interarm sources, which may reflect the molecular-cloud properties in and out of spiral arms.

After positionally matching the compact sources with young stellar objects from the Hi-GAL survey (Elia et al. 2017, 2021), the sample was split into prestellar and protostellar sources, and the star formation properties were investigated. The radii and column densities of prestellar sources were found to be systematically lower than protostellar clumps. The mass—radius relationships for these two samples agree with each other, and both slopes are consistent with the slopes found in quiescent molecular clouds in an external galactic system (Querejeta et al. 2021).
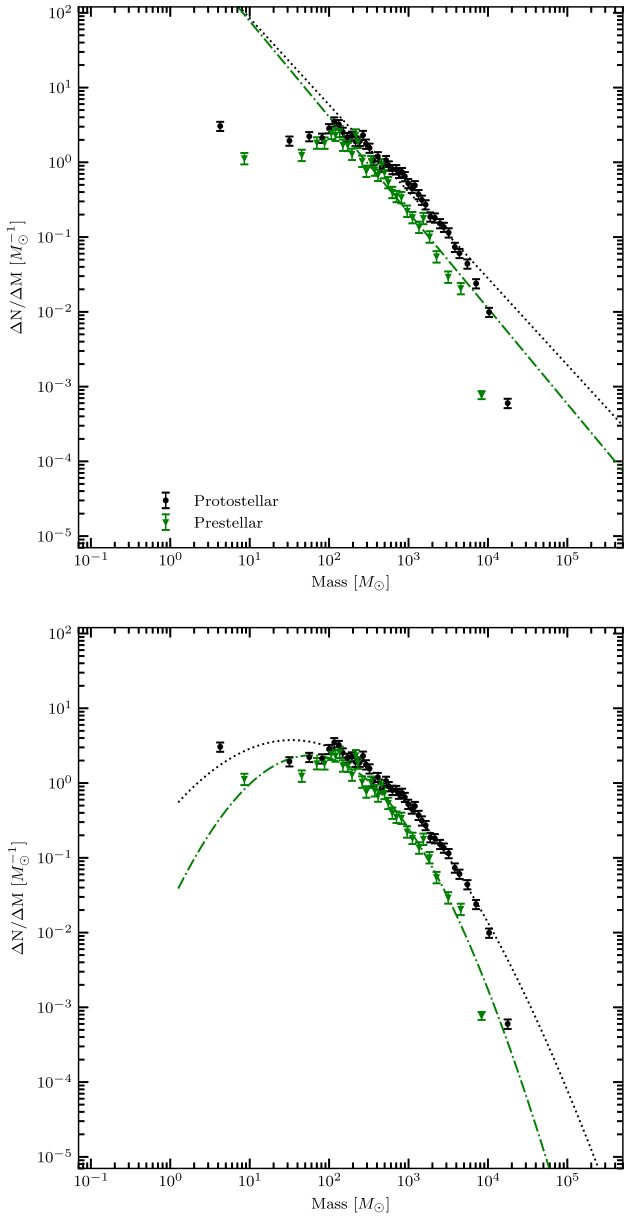
**Figure 9.** The clump-mass distributions of the protostellar (black circles) and prestellar (green triangles) compact sources. The fits are represented by the black dotted and green dot–dashed lines, respectively with the least-square fits in the top panel, on the assumption of a power law, and the bottom panel displaying lognormal fits.

*L/M* ratios of both individual clumps and globally across the Galactic Plane do not show significant variations as a function of Galactic environment. The mean values found are an order of magnitude lower than those in other Galactic-scale studies, hinting at the lower star-forming content of PGCCs.

Finally, a comparison of ATLASGAL sources (Schuller et al. 2009; Urquhart et al. 2018) associated with a PGCC and those not associated was made. The temperatures, column densities, and *L/M* ratios of the two samples were found to be not drawn from the same population, with lower temperatures, lower *L/M* ratios, and higher column densities for PGCC-associated sources, confirming PGCCs form a distinct population of Galactic sources.
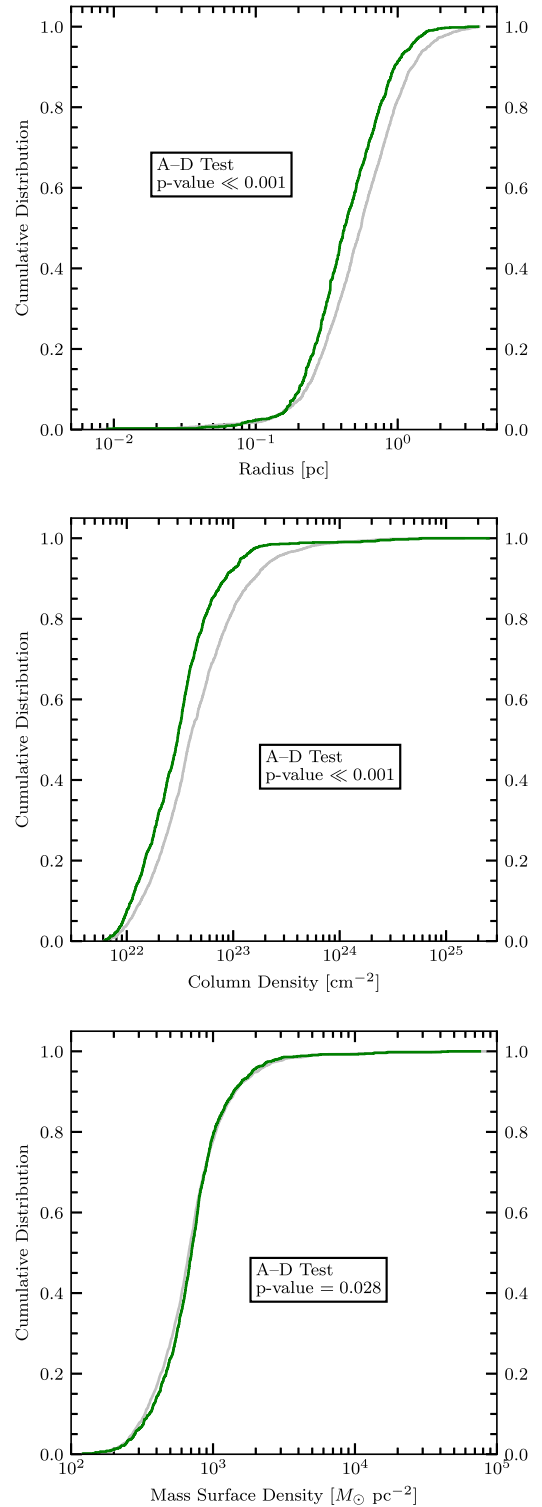
**Figure 10.** Cumulative distributions of the compact source radii (top), column densities (middle), and surface densities (bottom) for the protostellar (grey) and prestellar (green) samples.
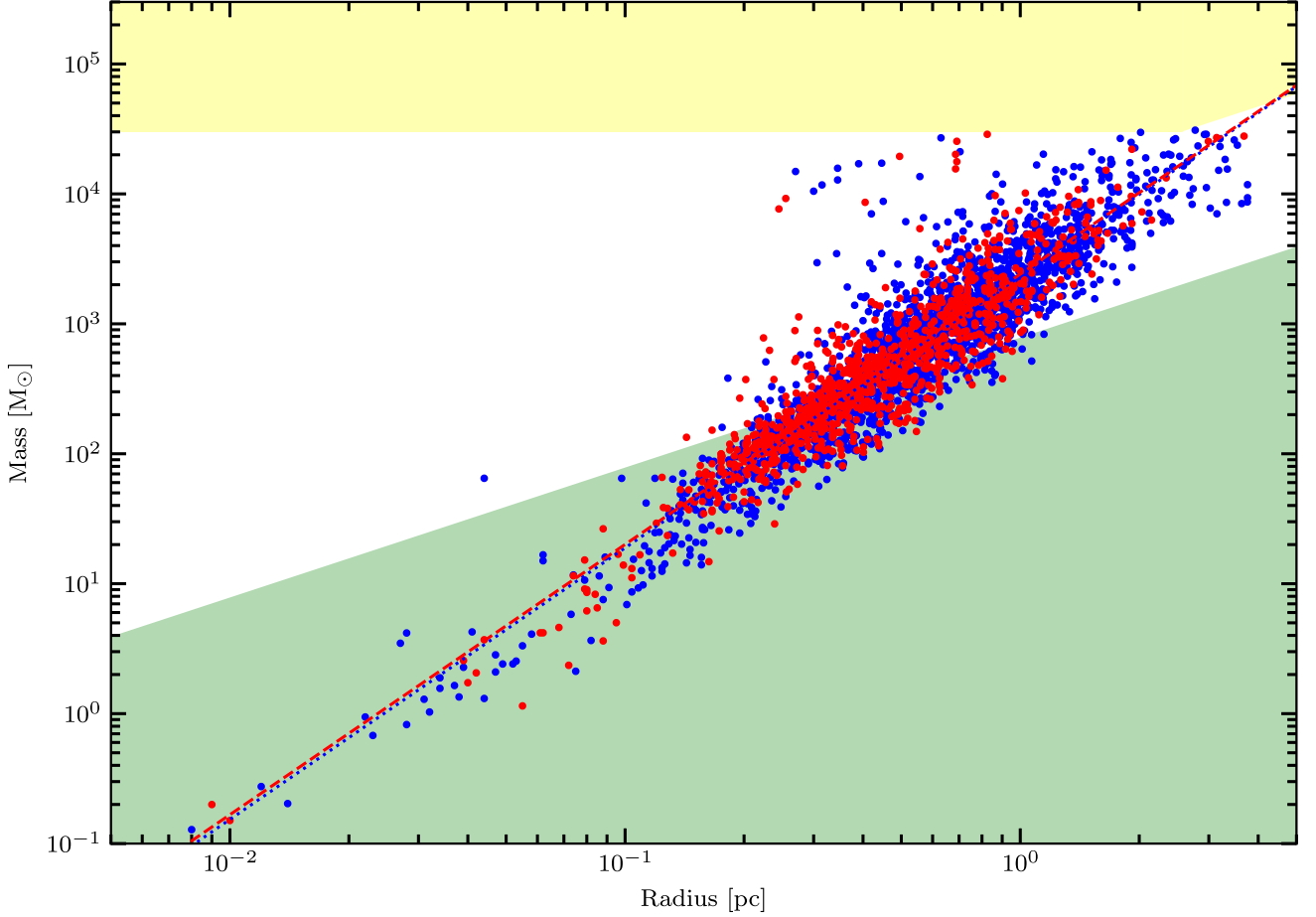
**Figure 11.** The mass–radius relationship for the SCOPE compact sources. The protostellar sources are indicated by the blue circles, and the prestellar represented by the red circles. The blue dotted and red dashed lines represent least-squares linear fits to the proto and prestellar samples with slopes of $2.089 \pm 0.019$ and $2.083 \pm 0.028$, respectively. The green region represents the parameter space where massive star formation does not occur, satisfying the relationship $m(r) \leq 580 \, \mathrm{M}_\odot (R_{\mathrm{eff}}/\mathrm{pc})^{1.33}$ (Kauffmann & Pillai 2010). The yellow region at the upper end of the plot is where young massive clusters would be found Bressert et al. (2012).

**Table 7.** Statistics for $L/M$ in the Hi-GAL-associated, star-forming compact-source sample (first row), and the individual spiral-arm subsets. The mean ($\bar{x}$), standard error, standard deviation ($\sigma$), median, and Anderson–Darling $p$-values are given.

| Spiral arm | $\bar{x}$ | $\frac{\sigma}{\sqrt{N}}$ | $\sigma$ | Median | A–D $p$-value |
|---|---|---|---|---|---|
| **Total** | 0.73 | 0.05 | 2.09 | 0.24 | |
| Scutum–Centaurus | 0.80 | 0.06 | 2.00 | 0.24 | $\gg 0.250$ |
| Sagittarius | 0.75 | 0.09 | 2.14 | 0.21 | $\gg 0.250$ |
| Perseus | 0.71 | 0.12 | 1.84 | 0.26 | $\gg 0.250$ |
| Local | 0.62 | 0.18 | 2.14 | 0.19 | 0.029 |
| Outer | 1.49 | 0.39 | 2.70 | 0.46 | $\ll 0.001$ |
| Interarm | 0.90 | 0.22 | 2.50 | 0.27 | 0.209 |

**Figure 12.** Cumulative distributions of the luminosity-to-mass ratio for individual compact sources in the whole PGCC sample and the separate spiral arms. The colours are as described in Fig. 8.
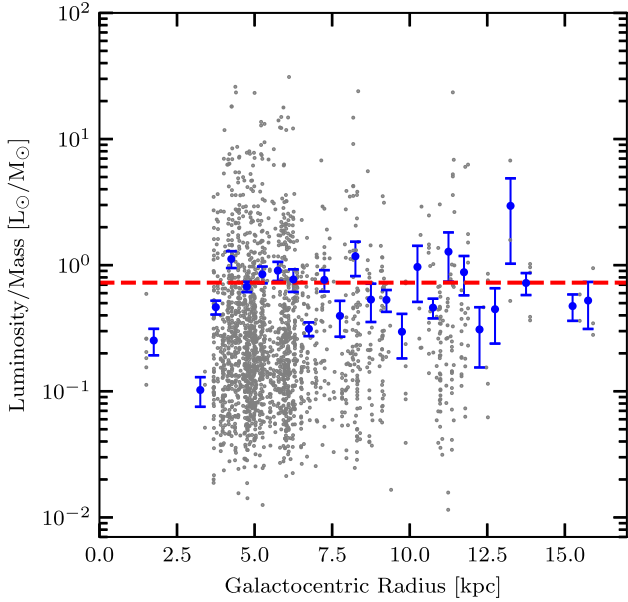
**Figure 13.** *L/M* as a function of Galactocentric radius. The individual compact sources are displayed by the grey circles. The blue circles are the averages in 0.5-kpc bins, with the associated standard error on the mean. The red horizontal dashed line indicates the Galactic average of 0.73 $L_\odot/M_\odot$.
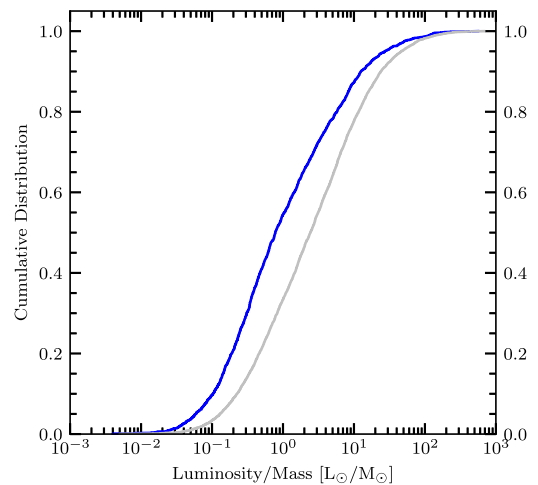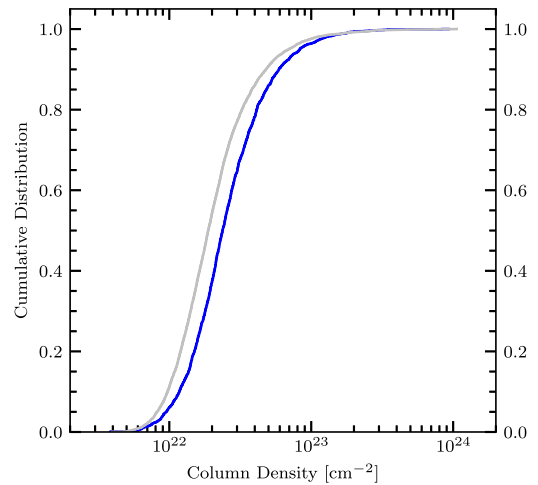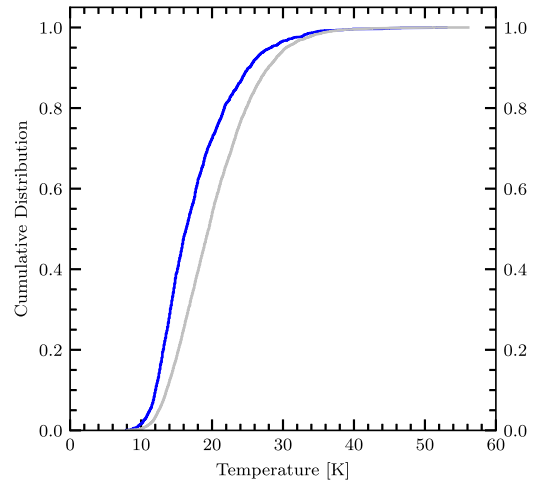
**Figure 14.** Cumulative distributions of ATLASGAL sources associated with PGCCs (blue) and those not associated (grey). The plots are temperature, column density, and *L/M* in the top, middle, and bottom panels, respectively.

to have the opportunity to conduct observations from this mountain. This research made use of the data from the Milky Way Imaging Scroll Painting (MWISP) project, which is a multiline survey in 12CO/13CO/C18O along the northern Galactic Plane with PMO-13.7m telescope. We are grateful to all the members of the MWISP working group, particularly the staff members at PMO-13.7m telescope, for their long-term support. MWISP was sponsored by National Key R&D Program of China with grant 2017YFA0402701 and CAS Key Research Program of Frontier Sciences with grant QYZDJ-SSW-SLH047. This research has made use of NASA's Astrophysics Data System. The Starlink software (Currie et al. 2014) is currently supported by the East Asian Observatory.

## DATA AVAILABILITY

The SCOPE survey and its data products are described fully in Liu et al. (2018) and Eden et al. (2019). The JPS and its images and source catalogue can be found in Eden et al. (2017). The associated download instructions are within those papers, or per request to the lead author.

The proposal IDs for these projects can be used to download raw observation data (both surveys) or reduced data products (SCOPE only) from the Canadian Astronomy Data Centre's JCMT Science Archive. The JPS proposal ID is MJLSJ02, whilst the SCOPE survey data can be found with: MJLSY14B, M15AI05, M15BI06, and M16AL003.

## REFERENCES

Anderson L. D., Bania T. M., 2009, ApJ, 690, 706
Benjamin R. A., 2008, in Beuther H., Linz H., Henning T.eds, ASP Conf. Ser. Vol. 387, Massive Star Formation: Observations Confront Theory. Astron. Soc. Pac., San Francisco, p. 375
Berdikhan. D. et al., 2024, A&A, 684, A144
Berry D. S., 2015, Astron. Comput., 10, 22
Billington S. J. et al., 2019, MNRAS, 490, 2779
Bintley D. et al., 2014, in Proc. SPIE Conf. Ser. Vol. 9153, Millimeter, Submillimeter, and Far-Infrared Detectors and Instrumentation for Astronomy VII. SPIE, Bellingham, p. 915303
Brand J., Blitz L., 1993, A&A, 275, 67
Bressert E., Ginsburg A., Bally J., Battersby C., Longmore S., Testi L., 2012, ApJ, 758, L28
Chrysostomou A., 2010, Highlights Astron., 15, 797
Colombo D. et al., 2022, A&A, 658, A54
Currie M. J., Berry D. S., Jenness T., Gibb A. G., Bell G. S., Draper P. W., 2014, in Manset N., Forshay P.eds, ASP Conf. Ser. Vol. 485, Astronomical Data Analysis Software and Systems XXIII. Astron. Soc. Pac., San Francisco, p. 391
Dame T. M., Hartmann D., Thaddeus P., 2001, ApJ, 547, 792
Dempsey J. T., Thomas H. S., Currie M. J., 2013, ApJS, 209, 8
Dobbs C. L., Burkert A., Pringle J. E., 2011, MNRAS, 417, 1318
Duarte-Cabral A. et al., 2021, MNRAS, 500, 3027
Dunham M. K., Rosolowsky E., Evans Neal J. I., Cyganowski C., Urquhart J. S., 2011, ApJ, 741, 110
Dutta S. et al., 2020, ApJS, 251, 20
Dutta S. et al., 2022, ApJ, 931, 130
Dutta S. et al., 2024, AJ, 167, 72
Eden D. J., Moore T. J. T., Plume R., Morgan L. K., 2012, MNRAS, 422, 3178
Eden D. J., Moore T. J. T., Morgan L. K., Thompson M. A., Urquhart J. S., 2013, MNRAS, 431, 1587
Eden D. J., Moore T. J. T., Urquhart J. S., Elia D., Plume R., Rigby A. J., Thompson M. A., 2015, MNRAS, 452, 289
Eden D. J. et al., 2017, MNRAS, 469, 2163
Eden D. J. et al., 2018, MNRAS, 477, 3369
Eden D. J. et al., 2019, MNRAS, 485, 2895
Eden D. J. et al., 2020, MNRAS, 498, 5936
Eden D. J. et al., 2021, MNRAS, 500, 191
Elia D. et al., 2017, MNRAS, 471, 100
Elia D. et al., 2021, MNRAS, 504, 2742
Fehér O. et al., 2022, ApJS, 258, 17
Giannetti A., Wyrowski F., Leurini S., Urquhart J., Csengeri T., Menten K. M., Bronfman L., van der Tak F. F. S., 2015, A&A, 580, L7
Ginsburg A., Bressert E., Bally J., Battersby C., 2012, ApJ, 758, L29
Hirano N. et al., 2024, ApJ, 961, 123
Holland W. S. et al., 2013, MNRAS, 430, 2513
Jackson J. M. et al., 2006, ApJS, 163, 145
Jhan K.-S. et al., 2022, ApJ, 931, L5
Juvela M. et al., 2018, A&A, 612, A71
Kalberla P. M. W. et al., 2010, A&A, 521, A17
Kauffmann J., Pillai T., 2010, ApJ, 723, L7
Kauffmann J., Bertoldi F., Bourke T. L., Evans N. J. I., Lee C. W., 2008, A&A, 487, 993
Kauffmann J., Pillai T., Shetty R., Myers P. C., Goodman A. A., 2010, ApJ, 716, 433
Kim G. et al., 2020, ApJS, 249, 33
Koda J. et al., 2012, ApJ, 761, 41
Kolpak M. A., Jackson J. M., Bania T. M., Clemens D. P., Dickey J. M., 2003, ApJ, 582, 756
Kruijssen J. M. D., Longmore S. N., 2013, MNRAS, 435, 2598
Krumholz M. R., Klein R. I., McKee C. F., 2011, ApJ, 740, 74
Larson R. B., 1981, MNRAS, 194, 809
Leung H. O., Thaddeus P., 1992, ApJS, 81, 267
Liu T., Wu Y., Zhang H., 2013, ApJ, 775, L2
Liu T. et al., 2016, ApJ, 829, 59
Liu T. et al., 2018, ApJS, 234, 28
Longmore S. N. et al., 2017, MNRAS, 470, 1462
MacKenzie T. et al., 2011, MNRAS, 415, 1950
Maíz Apellániz J., Úbeda L., 2005, ApJ, 629, 873
Mannfors E. et al., 2021, A&A, 654, A123
May J., Bronfman L., Alvarez H., Murphy D. C., Thaddeus P., 1993, A&AS, 99, 105
McClure-Griffiths N. M. et al., 2009, ApJS, 181, 398
Mège P. et al., 2021, A&A, 646, A74
Mitchell G. F., Johnstone D., Moriarty-Schieven G., Fich M., Tothill N. F. H., 2001, ApJ, 556, 215
Molinari S., Pezzuto S., Cesaroni R., Brand J., Faustini F., Testi L., 2008, A&A, 481, 345
Molinari S. et al., 2010, A&A, 518, L100
Molinari S. et al., 2016, A&A, 591, A149
Moore T. J. T., Urquhart J. S., Morgan L. K., Thompson M. A., 2012, MNRAS, 426, 701
Moore T. J. T. et al., 2015, MNRAS, 453, 4264
Netopil M., Oralhan İ. A., Çakmak H., Michel R., Karataş Y., 2022, MNRAS, 509, 421
Nettke W. et al., 2017, MNRAS, 468, 250
Park G. et al., 2023, ApJS, 264, 16
Pelkonen V. M., Padoan P., Haugbølle T., Nordlund Å., 2021, MNRAS, 504, 1219
Peretto N., Fuller G. A., 2009, A&A, 505, 405
Peretto N., Fuller G. A., 2010, ApJ, 723, 555
Planck Collaboration XXIII, 2011, A&A, 536, A23
Planck Collaboration XI, 2014, A&A, 571, A11
Planck Collaboration XXVIII, 2016, A&A, 594, A28
Popescu C. C., Yang R., Tuffs R. J., Natale G., Rushton M., Aharonian F., 2017, MNRAS, 470, 2539
Portegies Zwart S. F., McMillan S. L. W., Gieles M., 2010, ARA&A, 48, 431
Querejeta M. et al., 2021, A&A, 645, A97
Ragan S. E., Moore T. J. T., Eden D. J., Hoare M. G., Elia D., Molinari S., 2016, MNRAS, 462, 3123
Ragan S. E., Moore T. J. T., Eden D. J., Hoare M. G., Urquhart J. S., Elia D., Molinari S., 2018, MNRAS, 479, 2361

Rani R., Moore T. J. T., Eden D. J., Rigby A. J., Duarte-Cabral A., Lee Y.-N., 2023, MNRAS, 523, 1832

Reed B. C., 2000, AJ, 120, 314

Reid M. J. et al., 2014, ApJ, 783, 130

Reid M. J., Dame T. M., Menten K. M., Brunthaler A., 2016, ApJ, 823, 77

Reid M. J. et al., 2019, ApJ, 885, 131

Rigby A. J. et al., 2016, MNRAS, 456, 2885

Rigby A. J. et al., 2019, A&A, 632, A58

Roman-Duval J., Jackson J. M., Heyer M., Johnson A., Rathborne J., Shah R., Simon R., 2009, ApJ, 699, 1153

Sahu D. et al., 2021, ApJ, 907, L15

Sahu D. et al., 2023, ApJ, 945, 156

Schisano E. et al., 2020, MNRAS, 492, 5420

Schuller F. et al., 2009, A&A, 504, 415

Schuller F. et al., 2017, A&A, 601, A124

Schuller F. et al., 2021, MNRAS, 500, 3064

Simpson R. J., Nutter D., Ward-Thompson D., 2008, MNRAS, 391, 205

Sormani M. C., Barnes A. T., 2019, MNRAS, 484, 1213

Stark A. A., Lee Y., 2006, ApJ, 641, L113

Stil J. M. et al., 2006, AJ, 132, 1158

Su Y. et al., 2019, ApJS, 240, 9

Tang M. et al., 2018, ApJ, 856, 141

Tatematsu K. et al., 2021, ApJS, 256, 25

Umemoto T. et al., 2017, PASJ, 69, 78

Urquhart J. S. et al., 2007, A&A, 474, 891

Urquhart J. S. et al., 2009, A&A, 507, 795

Urquhart J. S. et al., 2011, MNRAS, 410, 1237

Urquhart J. S. et al., 2012, MNRAS, 420, 1656

Urquhart J. S. et al., 2013, MNRAS, 435, 400

Urquhart J. S., Figura C. C., Moore T. J. T., Hoare M. G., Lumsden S. L., Mottram J. C., Thompson M. A., Oudmaijer R. D., 2014a, MNRAS, 437, 1791

Urquhart J. S. et al., 2014b, MNRAS, 443, 1555

Urquhart J. S. et al., 2015, MNRAS, 452, 4029

Urquhart J. S. et al., 2018, MNRAS, 473, 1059

Urquhart J. S. et al., 2021, MNRAS, 500, 3050

Urquhart J. S. et al., 2022, MNRAS, 510, 3389

Weidner C., Kroupa P., Bonnell I. A. D., 2010, MNRAS, 401, 275

Wienen M. et al., 2015, A&A, 579, A91

Wu Y., Liu T., Meng F., Li D., Qin S.-L., Ju B.-G., 2012, ApJ, 756, 76

Xu F. et al., 2024, ApJ, 963, L9

Yi H.-W. et al., 2018, ApJS, 236, 51

Yi H.-W., Lee J.-E., Kim K.-T., Liu T., Lim B., Tatematsu K., Jcmt Large Program 'Scope' Collaboration, 2021, ApJS, 254, 14

Yuan J. et al., 2016, ApJ, 820, 37

Zhang T., Wu Y., Liu T., Meng F., 2016, ApJS, 224, 43

Zhang C.-P. et al., 2018, ApJS, 236, 49

## SUPPORTING INFORMATION

Supplementary data are available at *MNRAS* online.

**suppl_data**

Please note: Oxford University Press is not responsible for the content or functionality of any supporting materials supplied by the authors. Any queries (other than missing material) should be directed to the corresponding author for the article.

[1] *Armagh Observatory and Planetarium, College Hill, Armagh BT61 9DB, UK*

[2] *Shanghai Astronomical Observatory, Chinese Academy of Sciences, 80 Nandan Road, Shanghai 200030, People's Republic of China*

[3] *Astrophysics Research Institute, Liverpool John Moores University, Liverpool Science Park, iC2, 146 Brownlow Hill. Liverpool L3 5RF, UK*

[4] *NRC Herzberg Astronomy and Astrophysics, 5071 West Saanich Rd, Victoria, BC V9E 2E7, Canada*

[5] *Department of Physics and Astronomy, University of Victoria, Victoria, BC V8W 2Y2, Canada*

[6] *Jodrell Bank Centre for Astrophysics, School of Physics and Astronomy, The University of Manchester, Oxford Road, Manchester M13 9PL, UK*

[7] *Korea Astronomy and Space Science Institute, 776 Daedeokdae-ro, Yuseong-gu, Daejeon 34055, Republic of Korea*

[8] *University of Science and Technology, Korea (UST), 217 Gajeong-ro, Yuseong-gu, Daejeon 34113, Republic of Korea*

[9] *National Astronomical Observatories, Chinese Academy of Sciences, Beijing 100012, China*

[10] *Key Laboratory of Radio Astronomy, Chinese Academy of Science, Nanjing 210008, China*

[11] *Academia Sinica Institute of Astronomy and Astrophysics, 11F of AS/NTU Astronomy – Mathematics Building, No.1, Section 4, Roosevelt Rd, Taipei 10617, Taiwan*

[12] *Department of Physics and Astronomy, University of Calgary, 2500 University Drive NW, Calgary, Alberta T2N 1N4, Canada*

[13] *Nobeyama Radio Observatory, National Astronomical Observatory of Japan, National Institutes of Natural Sciences, Nobeyama, Minamimaki, Minamisaku, Nagano 384-1305, Japan*

[14] *Astronomical Science Program, Graduate Institute for Advanced Studies, SOKENDAI, 2-21-1 Osawa, Mitaka, Tokyo 181-8588, Japan*

[15] *School of Physics and Astronomy, University of Leeds, Leeds LS2 9JT, UK*

[16] *Department of Astronomy, Peking University, 100871 Beijing China*

[17] *Astronomy Department, Universidad de Chile, Casilla 36-D, Santiago 7591245, Chile*

[18] *Department of Physics and Astronomy, James Madison University, MSC 4502, 901 Carrier Drive, Harrisonburg, VA 22807, USA*

[19] *RAL Space, STFC Rutherford Appleton Laboratory, Chilton, Didcot, Oxfordshire OX11 0QX, UK*

[20] *East Asian Observatory, 660 North A'ohōkū Place, Hilo, HI 96720, USA*

[21] *Jet Propulsion Laboratory, California Institute of Technology, 4800 Oak Gove Drive, Pasadena, CA 91109, USA*

[22] *Department of Physics, University of Helsinki, P.O. Box 64, FI-00014, Finland*

[23] *Institute of Astronomy, National Tsing Hua University, No. 101, Section 2, Kuang-Fu Road, Hsinchu 30013, Taiwan*

[24] *Center for Informatics and Computation in Astronomy, National Tsing Hua University, No. 101, Section 2, Kuang-Fu Road, Hsinchu 30013, Taiwan*

[25] *Department of Physics, National Tsing Hua University, No. 101, Section 2, Kuang – Fu Road, Hsinchu 30013, Taiwan*

[26] *Department of Physics and Astronomy, University College London, WC1E 6BT London, UK*

[27] *INAF – Osservatorio Astronomico di Trieste, Via G.B. Tiepolo 11, I-34143 Trieste, Italy*

[28] *Gemini Observatory/NSF's NOIRLab, 670 N. A'ohoku Place, Hilo, HI 96720, USA*

[29] *National Astronomical Observatory of Japan, National Institutes of Natural Sciences, 2-21-1 Osawa, Mitaka, Tokyo 181-8588, Japan*

[30] *Astronomical Science Program, Graduate Institute for Advanced Studies, SOKENDAI, 2-21-1 Osawa, Mitaka, Tokyo 181-8588, Japan*

[31] *IAPS – INAF, Via Fosso del Cavaliere, 100, I-00133 Rome, Italy*

[32] *Centre for Astrophysics and Planetary Science, University of Kent, Canterbury CT2 7NH, UK*

[33] *Oststrasse 15, D-51674 Wiehl, Germany*

[34] *School of Physical Sciences, The Open University, Walton Hall, Milton Keynes MK7 6AA, UK*

[35] *National Astronomical Research Institute of Thailand (Public Organization), 260 Moo 4, T. Donkaew, A. Maerim, Chiangmai 50180, Thailand*

This paper has been typeset from a TeX/LaTeX file prepared by the author.